



HAL
open science

Fate of antimony contamination generated by road traffic – A focus on Sb geochemistry and speciation in stormwater ponds

M. Philippe, Pierre Le Pape, E. Resongles, G. Landrot, R. Freydier, L. Bordier, B. Baptiste, L. Delbes, C. Baya, C. Casiot, et al.

► To cite this version:

M. Philippe, Pierre Le Pape, E. Resongles, G. Landrot, R. Freydier, et al.. Fate of antimony contamination generated by road traffic – A focus on Sb geochemistry and speciation in stormwater ponds. Chemosphere, 2023, 313, pp.137368. 10.1016/j.chemosphere.2022.137368 . hal-03874871

HAL Id: hal-03874871

<https://hal.science/hal-03874871>

Submitted on 28 Nov 2022

HAL is a multi-disciplinary open access archive for the deposit and dissemination of scientific research documents, whether they are published or not. The documents may come from teaching and research institutions in France or abroad, or from public or private research centers.

L'archive ouverte pluridisciplinaire **HAL**, est destinée au dépôt et à la diffusion de documents scientifiques de niveau recherche, publiés ou non, émanant des établissements d'enseignement et de recherche français ou étrangers, des laboratoires publics ou privés.

Journal Pre-proof

Fate of antimony contamination generated by road traffic – A focus on Sb geochemistry and speciation in stormwater ponds

M. Philippe, P. Le Pape, E. Resongles, G. Landrot, R. Freydier, L. Bordier, B. Baptiste, L. Delbes, C. Baya, C. Casiot, S. Ayrault



PII: S0045-6535(22)03861-9

DOI: <https://doi.org/10.1016/j.chemosphere.2022.137368>

Reference: CHEM 137368

To appear in: *ECSN*

Received Date: 29 August 2022

Revised Date: 9 November 2022

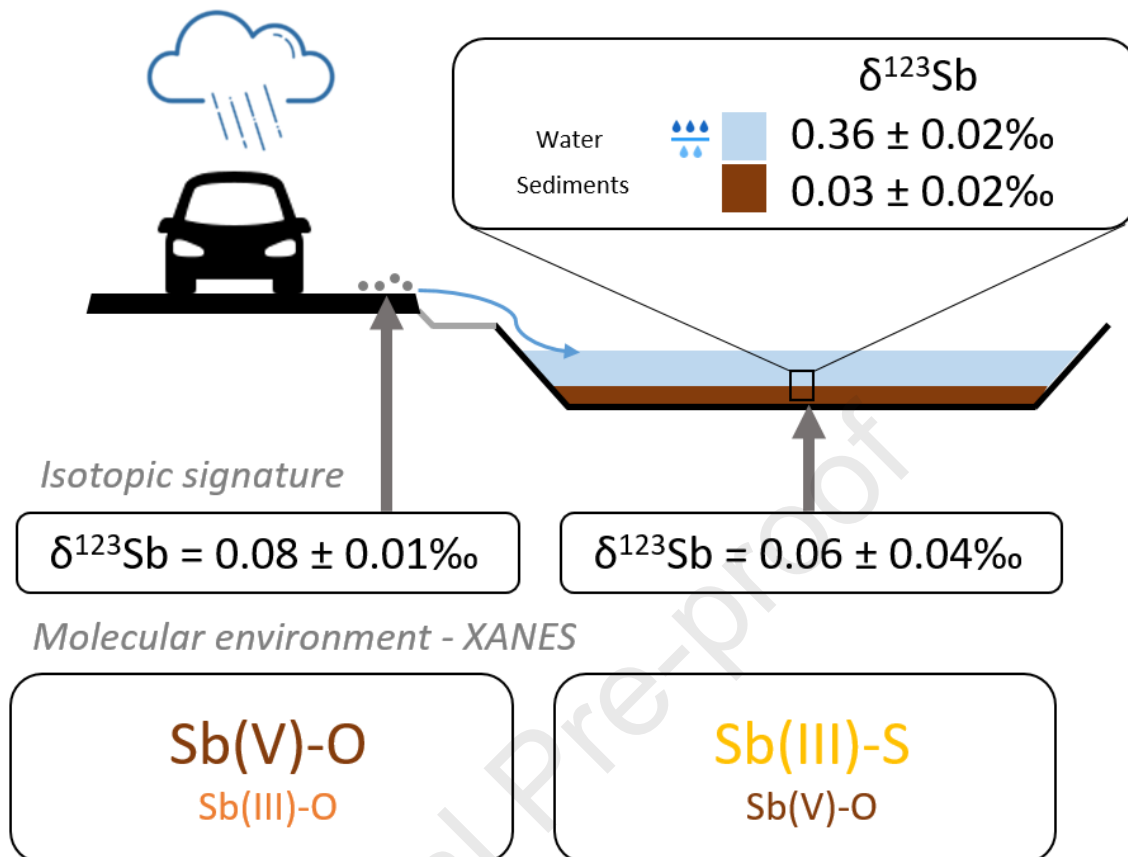
Accepted Date: 21 November 2022

Please cite this article as: Philippe, M., Le Pape, P., Resongles, E., Landrot, G., Freydier, R., Bordier, L., Baptiste, B., Delbes, L., Baya, C., Casiot, C., Ayrault, S., Fate of antimony contamination generated by road traffic – A focus on Sb geochemistry and speciation in stormwater ponds, *Chemosphere* (2022), doi: <https://doi.org/10.1016/j.chemosphere.2022.137368>.

This is a PDF file of an article that has undergone enhancements after acceptance, such as the addition of a cover page and metadata, and formatting for readability, but it is not yet the definitive version of record. This version will undergo additional copyediting, typesetting and review before it is published in its final form, but we are providing this version to give early visibility of the article. Please note that, during the production process, errors may be discovered which could affect the content, and all legal disclaimers that apply to the journal pertain.

© 2022 Published by Elsevier Ltd.

Maëva Philippe: Conceptualization, Methodology, Investigation, Formal analysis, Writing - Original Draft, Writing - Review & Editing - **Pierre Le Pape:** Conceptualization, Methodology, Investigation, Formal analysis, Writing - Original Draft, Writing - Review & Editing, Supervision - **Éléonore Resongles:** Investigation, Formal analysis, Writing - Review & Editing - **Gautier Landrot:** Investigation, Software, Writing - Review & Editing - **Rémi Freydier:** Investigation, Formal analysis - **Ludovic Delbes:** Investigation - **Louise Bordier:** Investigation, Formal analysis, Writing - Review & Editing - **Benoît Baptiste:** Software, Investigation - **Camille Baya:** Investigation - **Corinne Casiot:** Methodology, Writing - Review & Editing - **Sophie Ayrault:** Conceptualization, Methodology, Investigation, Formal analysis, Writing - Original Draft, Writing - Review & Editing, Project administration, Supervision.



1 **Fate of antimony contamination generated by road traffic – A focus on Sb geochemistry**
2 **and speciation in stormwater ponds**

3

4 Philippe M.^{1,2}, Le Pape P.², Resongles E.³, Landrot G.⁴, Freydier R.³, Bordier L.¹, Baptiste B.
5 ², Delbes L.², Baya C.², Casiot C.³, and Ayrault S.¹

6

7

8

9

¹ Laboratoire des Sciences du Climat et de l'Environnement (LSCE-IPSL), UMR 8212
10 (CEA/CNRS/UVSQ), Université Paris-Saclay, Gif-sur-Yvette, France

11

12

13

² Institut de Minéralogie, de Physique des Matériaux et de Cosmochimie (IMPMC), UMR
14 7590 CNRS – Sorbonne Université – IRD – MNHN, 4 place Jussieu, 75252 Paris Cedex 5,
15 France

16

17

³ HydroSciences Montpellier (HSM), Université de Montpellier - CNRS - IRD, Montpellier,
18 France

19

20

⁴ Synchrotron SOLEIL, F-91192 Gif-Sur-Yvette, France

21

22

23

24

25

26

Corresponding author: maeva.philippe@lsce.ipsl.fr - +33(0)602506084

27 **Highlights**

- 28
- Highway stormwater ponds concentrate Sb contamination from road runoff
- 29
- Sb isotopic composition of stormwater pond sediments is close to that of road dusts
- 30
- Sb(V)-O, Sb(III)-O, and Sb(III)-S species occur in the road-to-pond continuum
- 31
- Sb(III)-S species are observed as a specific signature of underwater reduced samples
- 32
- Sb speciation changes along the waterway show the high geochemical reactivity of Sb

33

Journal Pre-proof

34 **Abstract**

35 Although antimony (Sb) contamination has been documented in urban areas, knowledge gaps
36 remain concerning the contributions of the different sources to the Sb urban biogeochemical
37 cycle, including non-exhaust road traffic emissions, urban materials leaching/erosion and
38 waste incineration. Additionally, details are lacking about Sb chemical forms involved in urban
39 soils, sediments and water bodies. Here, with the aim to document the fate of metallic
40 contaminants emitted through non-exhaust traffic emissions in urban aquatic systems, we
41 studied trace element contamination, with a particular focus on Sb geochemistry, in three
42 highway stormwater pond systems, standing as models of surface environments receiving
43 road-water runoff. In all systems, differentiated on the basis of lead isotopic signatures, Sb
44 shows the higher enrichment factor with respect to the geochemical background, up to 130,
45 compared to other traffic-related inorganic contaminants (Co, Cr, Ni, Cu, Zn, Cd, Pb).
46 Measurements of Sb isotopic composition ($\delta^{123}\text{Sb}$) performed on solid samples, including air-
47 exposed dusts and underwater sediments, show an average signature of $0.07 \pm 0.05\text{‰}$ ($n=25$,
48 all sites), close to the $\delta^{123}\text{Sb}$ value measured previously in certified reference material of road
49 dust (BCR 723, $\delta^{123}\text{Sb} = 0.03 \pm 0.05\text{‰}$). Moreover, a fractionation of Sb isotopes is observed
50 between solid and dissolved phases in one sample ($n=3$ samples), which might result from Sb
51 (bio)reduction and/or adsorption processes. SEM-EDXS investigations show the presence of
52 discrete submicrometric particles concentrating Sb in all the systems, interpreted as friction
53 residues of Sb-containing brake pads. Sb solid speciation determined by linear combination
54 fitting of X-Ray Absorption Near Edge Structure (XANES) spectra at the Sb *K*-edge shows an
55 important spatial variability in the ponds, with Sb chemical forms likely driven by local redox
56 conditions: “dry” samples exposed to air exhibited contributions from Sb(V)-O (44% to 100%)
57 and Sb(III)-O (<10% to 56%) species whereas only underwater samples, representative of
58 suboxic/anoxic conditions, showed an additional contribution from Sb(III)-S (48% to 81%)
59 species. Altogether, these results confirm the traffic emission as a specific source of Sb
60 emission in surface environments. The spatial variations of Sb speciation observed likely

61 reflect an important geochemical reactivity in this context, which could have important
62 implications on Sb transfer properties in (sub)surface hydrosystems.

63

64 **Keywords:** antimony, road traffic contamination, stormwater ponds, Sb isotopes, Sb
65 speciation, Pb isotopes.

66

Journal Pre-proof

67 1. Introduction

68 Global-scale antimony (Sb) contamination has been recorded in ice cores since the
69 early 1900s (Krachler et al., 2005; Liu et al., 2021). In particular, the increase in Sb
70 concentrations has been interpreted as a rise of anthropogenic inputs related to waste
71 incineration and mining (Krachler et al., 2005; Liu et al., 2021). At the urban scale, different
72 sources contribute to the Sb biogeochemical cycle, including non-exhaust road traffic
73 emissions, urban materials leaching/erosion and waste incineration (Filella et al., 2009). In the
74 urban Orge River basin (Paris region, France), an increase in Sb enrichment factors in river
75 suspended particulate matters (SPM) has been persistently observed along the increasing
76 urbanization gradient (Le Pape et al., 2012; Froger et al., 2018). In Budapest (Hungary), Sb
77 atmospheric contamination has been observed in urban aerosols, showing extreme
78 enrichment factors, from 5,097 in PM₁₀ to 18,892 in PM₂, and were interpreted as resulting
79 from road traffic (Salma and Maenhaut, 2006). Indeed, road traffic is known to induce
80 emissions of inorganic contaminants due for instance to abrasion of brake pads (Von Uexküll
81 et al., 2005; Napier et al., 2008; Hu et al., 2017), namely copper (Cu), zinc (Zn), cadmium (Cd),
82 chromium (Cr) and Sb. In particular, Sb has been used in brake pads lubricants (Sb₂S₃) as
83 replacement for asbestos (Chan and Stachowiak, 2004; Lee et al., 2013). Additionally, metallic
84 trace element emissions are also reported as originating from tires and oils combustion or
85 leakage (Hjortenkrans et al., 2007; Davis et al., 2001; Johansson et al., 2009) and other urban
86 materials such as safety barriers, road paints or cigarette butts (Zhang et al., 2004; Moriwaki
87 et al., 2009; Kibblewhite, 2018; Turner and Filella, 2020). After their emission at the road scale,
88 these contaminants are transported by road runoff and potentially impact the quality of surface
89 waters (Helmreich et al., 2010; Le Pape et al., 2012; Wang et al., 2017; Froger et al., 2018).
90 Although traffic is generally mentioned as a major source of Sb in the urban environment
91 (Hjortenkrans et al., 2006; Johansson et al., 2009), its contribution to the global urban Sb
92 contamination is poorly quantified. Nonetheless, identification of the contributions of the
93 diverse sources and pathways of Sb contamination could lead to a better management of this

94 pervasive and persistent geochemical enrichment, for instance by adapting public policy to
95 control or remove part of these contamination sources.

96 Highway stormwater ponds, located along roads, are recognized as efficient accumulators
97 of road contaminations since they directly receive the runoff water leaching roads and other
98 surfaces contaminated by vehicles-related emissions (Hares and Ward, 1999; Clozel et al.,
99 2006; Hwang et al., 2016). Additionally, as some of these stormwater pond systems are
100 vegetated, and harbour sedimentary systems representative of urban soils and sediments,
101 they stand as interesting model hydrosystems (Stachel et al., 2010) to study the mechanism
102 of Sb accumulation from road emissions. While Cu, Zn, Cd, Cr and Pb concentrations from
103 measurements in road and street dusts are often reported in the literature (e.g. Ahmed and
104 Ishiga, 2006; Haus et al., 2007), Sb enrichment and chemistry have rarely been studied in
105 road-related environments, in particular in such stormwater pond systems. A few data are
106 currently available for road ponds, and only focusing on Sb contamination level based on the
107 measurements of its concentrations in bulk and dissolved fraction of pond water samples from
108 Germany, England, Sweden and Canada (up to $11 \mu\text{g}\cdot\text{L}^{-1}$ (Kamalakkannan et al., 2004;
109 Stachel et al., 2010; Nielsen et al., 2015; Perron and Pick, 2020)) and in sediments from a UK
110 motorway drainage pond ($1.44 - 2.01 \text{ mg}\cdot\text{kg}^{-1}$) (Kamalakkannan et al., 2004). However, neither
111 speciation nor isotopic measurements are currently available on these accumulating pond
112 system media, data which could be extended to surface media exposed to road emissions
113 such as urban areas in general.

114 To study the sources and the transfer pathways of contaminant-bearing particles, the
115 relative abundance in contaminant isotopes in both the aqueous and the solid phases has
116 proven to be an informative geochemical parameter (Monna et al., 1997). For instance, in
117 urban context, $^{208}\text{Pb}/^{206}\text{Pb}$ vs. $^{206}\text{Pb}/^{207}\text{Pb}$ ratios have been used as anthropogenic source
118 tracers in soils (Emmanuel and Erel, 2002), or to estimate the urban pressure exerted on urban
119 rivers (Ayrault et al., 2012; Le Pape et al., 2013). Indeed, Pb is a common and abundant
120 contaminant of urban environments, whose isotopic composition allows discriminating

121 between natural and anthropogenic sources for lead-bearing particles (Ayrault et al., 2012).
122 Comparatively, Sb isotopic signature has been scarcely used in the literature, and has never
123 been used to trace Sb contamination in the urban context. The pioneering study of Rouxel et
124 al. (2003) gives the first values of Sb fractionation between ^{123}Sb and ^{121}Sb for different natural
125 samples representative of diverse sources at the Earth surface, including seawater and main
126 geological rocks. This study also suggests that Sb isotopic fractionation could be a useful tracer
127 for biogeochemical processes affecting Sb, such as changes in oxidation state. More recently,
128 in environmental sciences, $\delta^{123}\text{Sb}$ has been used to trace the contributions from different Sb-
129 sources in mine-impacted streams (Resongles et al., 2015b). Thus, Sb isotopic signature has
130 a good potential for both discriminating the sources of Sb at the site scale and could also help
131 to trace the local biogeochemical processes involving changes of oxidation state, ligand
132 exchange, or adsorption onto natural particles (Ferrari et al., 2022; Zhou et al., 2022).

133 Determining the physico-chemical processes governing Sb mobility in surface
134 environments is essential to unravel the transfer pathways leading to the dissemination of this
135 toxic metalloid. As Sb is a redox sensitive element, Sb mobility is strongly driven by its
136 speciation in both the aqueous and the solid phases. In (sub-)surface soils and sediments, Sb
137 harbours two oxidation states, Sb(III) and Sb(V), the latter form presenting the higher solubility
138 (Johnston et al., 2020). Thus, determining Sb speciation is of prime importance to predict Sb
139 short- to long- term transfer properties. Currently, the few information on Sb speciation have
140 been obtained *via* chemical extractive methods applied to road soils, road dusts, and airborne
141 particles (Amereih et al., 2005; Quiroz et al., 2013; Sánchez-Rodas et al., 2017), showing
142 various contributions from both Sb(III) and Sb(V) species. Varrica et al. (2013) have measured
143 Sb speciation *via* X-ray Absorption Spectroscopy (XAS) at the Sb *K*-edge in various urban
144 particles, and observed a mix of Sb(V)-O, Sb(III)-O and Sb(III)-S molecular environments,
145 interpreted as directly resulting from brake pad friction and abrasion (Cho et al., 2006; Martinez
146 and Echeberria, 2016). Thus, a full comprehensive description of Sb speciation along the road-
147 to-pond continuum is necessary to determine whether Sb speciation is inherited from direct

148 traffic inputs or can be further influenced by local biogeochemical processes taking place in
149 surface soils and sediments.

150 Here, we have compared the level of trace metal contamination, including Sb, in three
151 stormwater pond systems along roads presenting high traffic volumes in the Ile-de-France
152 region (France). These sites are taken as model systems representative of surface
153 environment accumulating the contaminations from road traffic, which can be largely found in
154 urban areas (e.g. urban hydrosystems, rivers, wetlands). Additionally, the studied sites are
155 representative of different land uses (rural and urban) and of different chronologies of dust and
156 sediment deposition. Both sediments and waters were sampled in the road-to-pond continuum,
157 with the aim to reveal the spatial evolution of trace element contamination from emission to
158 deposition in near road environments. Thanks to a combination of techniques, including
159 contaminant concentration analyses (among them Cu, Cd, Cr, Ni, Pb, Sb, Zn), analysis of
160 relative abundance of Pb and Sb isotopes, and speciation analysis of Sb, we highlight key
161 steps of Sb biogeochemical cycle in surface environments impacted by road traffic. Thus, we
162 show that the level and type of contamination of pond systems is likely related to the nature of
163 drained surfaces (urban vs. rural) and extent of particle accumulation. Then, we identified a
164 specific $\delta^{123}\text{Sb}$ signature of highway stormwater pond samples, including road dusts and
165 sediments, which is shown to be close of that reported elsewhere for road dust. Finally, we
166 studied in detail the variations of Sb speciation by the mean of XANES at the Sb *K*-edge in
167 solid samples along the road-to-pond continuum, showing that Sb presents an important
168 geochemical reactivity, with multiple oxidation states and ligands involved as a function of the
169 local redox conditions.

170 **2. Materials and methods**

171 **2.1. Study sites**

172 The three highway stormwater pond systems studied are located in the south of Île-de-
173 France region in the Orge River watershed (Fig. SI-1.1). Previous researches performed in the
174 Orge River basin have provided a good knowledge of land use, geology, spatial and temporal

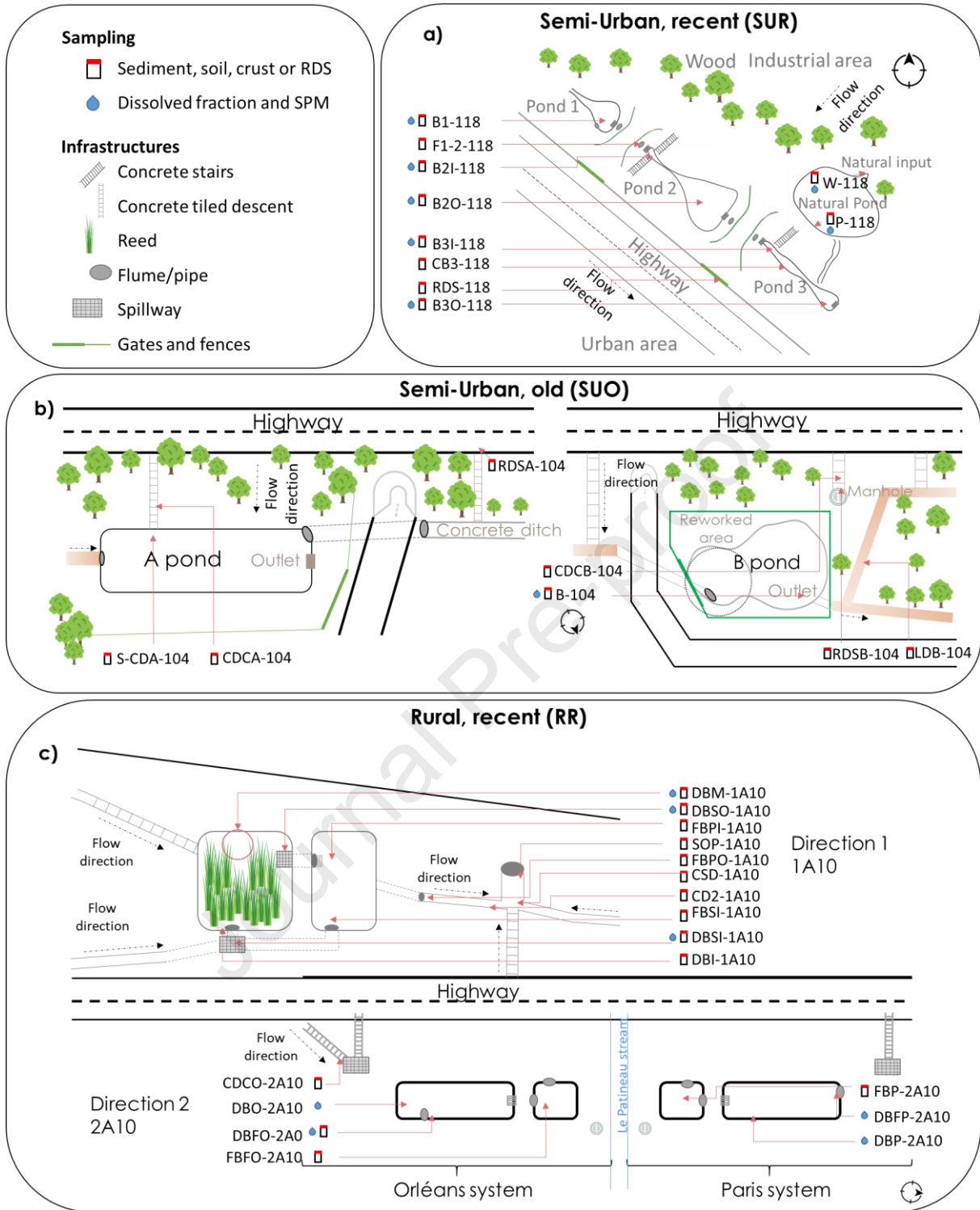
175 dynamics of contaminants of anthropogenic origin (e.g. metals and PAHs) (Le Pape et al.,
176 2012; Froger et al., 2018, 2019). The highway stormwater pond systems studied are different
177 by the nature of drained areas (urban + road, mostly road or 100% road) but also by their
178 design (decantation pond, filtration pond, presence or not of a polyethylene geomembrane)
179 and their construction date (Table 1). Road sections related to the studied stormwater ponds
180 have a high daily flux of ~50000 vehicles per day (Table 1). The presence of speed cameras
181 near both semi-urban systems should be noted because it induces braking and therefore the
182 emission of dust due to abrasion of brake pads. Three systems are studied: recent semi-urban
183 (SUR) situated in Orsay, old semi-urban (SUO) situated in Marcoussis, and recent rural (RR)
184 situated near Saint-Martin-de-Bréthencourt. Figure 1 represents the spatial organization of the
185 three stormwater pond systems. The SUR system is composed by 3 geomembrane isolated
186 ponds arranged in series and connected by rafts at their base and by nozzles in height for
187 overflows during important rain events. The first pond (B1) is located upstream and the third
188 (B3) downstream. Both B1 and B2 are planted with reeds while B3 is channeled and unplanted.
189 A “natural pond” (P) supplied by the upperlying aquifer of the Fontainebleau sands (W),
190 independent of the road runoff collection network but hydrologically connected to B3, is also
191 present. The SUO system is composed by 2 disconnected unplanted decantation ponds
192 situated in an urban area surrounded by crops. The “A” pond had been dredged a few days
193 before sampling while “B” pond has never been dredged since the pond construction (Figure
194 1). The RR system is divided in two sub-sites: “Direction 1” (1A10) composed by a
195 geomembrane isolated decantation pond planted with reefs in series with a dry filtration pond
196 and “Direction 2” (2A10) composed by two systems of unplanted geomembrane isolated
197 decantation ponds in series with dry filtration ponds. Waters from both sub-sites come from
198 the road through a spillway system.

199 **2.2. Sampling**

200 Sediments (S), concrete downhill crusts (CDC), road dust sediments (RDS), water samples
201 (dissolved fraction (W) and suspended particulate matters (P)) were sampled during the five

202 sampling campaigns carried out in January (2 campaigns) and February 2020 for SUR and
203 SUO systems and March and September 2020 for the RR system.

Journal Pre-proof



204

205 **Figure 1.** Layout of the three studied stormwater ponds systems. (a) Semi-Urban Recent
 206 system (SUR) of Orsay, (b) Semi-Urban Old system (SUO) of Marcoussis and (c) Rural Recent
 207 system (RR) of Saint-Martin-de-Bréthencourt. Sampling locations for each type of samples
 208 (water, SPM, sediment) are indicated on the schemes. Pots symbols stand for solid sampling,
 209 drops stand for water sampling (dissolved phase, <math><0.22 \mu\text{m}</math>) and suspended particulate
 210 matters (SPM > 0.3 μm) sampling.

211

212 **Table 1.** Characteristics of the highway stormwater pond systems (year of construction, type
 213 of pond conception, type of drained surfaces, traffic intensity and presence of speed cameras)

Denomination	GPS coordinates	Construction (year)	Type	Drained surface	Traffic per day (2017)	Presence of speed camera
Semi-urban, recent (SUR)	48.7115, 2.1863	~2000	Decantation	Urban + Road	54,187	Yes
Semi-urban, old (SUO)	48.6334, 2.2246	1990s	Decantation	Road	56,595	Yes
	48.6320, 2.2292					
Rural, recent (RR)	48.5120, 1.9072	2012	Decantation + filtration	Road	42,225	No
	48.5125, 1.9082					

214

215 Underwater sediments were collected in 180 mL polypropylene containers tightly closed
 216 onsite and a water column was kept above the sediments to avoid direct contact with air. Such
 217 reduced sediments were then inserted as quickly as possible in a glove box at the IMPMC
 218 laboratory for further sample processing. Inside the glove box, the solid samples were
 219 separated from the liquid phase by centrifugation, dried under vacuum, and finally stored in
 220 anoxic conditions (N_2 , <5 ppm O_2). Dissolved fraction of the water samples was recovered by
 221 filtering to $0.22 \mu m$ with PES filters (Sartorius Minisart™) and acidified with ultrapure nitric acid
 222 (0.5 M) in 50 mL Falcon® tubes directly on site and further stored at $4^\circ C$. Bulk water (~ 2 L)
 223 was collected in PET bottles previously washed with HNO_3 0.5 N and rinsed on site with bulk
 224 water. Water pH, conductivity and temperature were measured onsite except for 2 samples in
 225 the RR pond system (15 water samples listed in Table SI-1.2). Road dust sediments (RDS)
 226 were collected on the road using a plastic spatula and placed in a tightly closed polyethylene
 227 bag (SUO system) or using a plastic brush and kept in a Falcon tube® (SUR system). Crusts
 228 were collected on the slope concrete tiles channeling water from the road to the pond with a
 229 plastic spatula and kept in a tightly closed polyethylene bag. RDS and crusts were stored at
 230 room temperature in the dark. Full information about the 41 solid samples (conditions of
 231 sampling, drying conditions, type and matrix) are listed in Table SI-1.1.

2.3. Sample preparation

2.3.1. Suspended particulate matter (SPM) and sediment

Within the hours following collection, SPM samples were obtained by filtration (in laboratory) of approximately 2 L of bulk water (sometime less when clogging occurred) through previously dried and weighted quartz filters (Pallflex® Tissuquartz™, retaining 99.9% of >0.3 µm particles) using glass or plastic tulips previously rinsed with 0.5 N nitric acid and a pump. The filtered volume was measured by weighting. After filtration, filters were dried under oxic conditions before total mineralization (Priadi et al., 2011). For multi-elemental analysis, approximately 100 mg of sediment, previously sieved at 2 mm with a plastic sieve, were crushed in an agate mortar before total mineralization (Le Pape et al., 2012).

2.3.2. Bulk mineralization

Total digestion of sediments and SPM was performed in three steps using ultrapure concentrated acids to avoid contaminations in open PTFE Savillex® vials: 4 mL of HF (47-51%) and 2 mL HClO₄ (67%) heated at 150 °C for 320 minutes, 3.75 mL of HCl (34-37%) and 1.25 mL of HNO₃ (67%) heated at 120°C for 180 minutes and finally heating at 110 °C with addition of 1 mL of HNO₃ (67%) for 55 minutes. Final solutions were transferred to 50 mL Falcon® (polyethylene) tubes, Savillex® vials rinsed three times by heating approximately 10 mL of HNO₃ 0.5 M and completed at 50 mL with 0.5 M nitric acid (Le Pape et al., 2012). Two certified reference materials (CRM), sediment SL1 and street dust BCR 723, were added in each mineralization batch. Blanks were performed in each batch and a filter blank was included in each SPM batches.

2.4. Analytical methods

2.4.1. Elemental analysis and enrichment factors calculation

The concentrations of 25 major, minor and trace elements were determined using triple quadrupole inductively coupled plasma – mass spectrometry (TQ-ICP-MS) (Thermo Scientific™ iCAP™ TQ) at LSCE laboratory (Tables SI-1.3, SI-1.4, SI-1.5). An internal

258 standard mixture (In, Ge, Rh and Re) was added on-line to the samples to correct for the
 259 instrumental sensitivity drift. Quality of analysis was checked using NIST 1640a (spring water)
 260 for dissolved samples, SL1 and BCR-723 for sediments (100 mg) and for SPM (10 mg) (Table
 261 SI-1.6). Accuracy was within $\pm 15\%$ of the certified values provided for the certified reference
 262 material SL1 and BCR 723 (except Ag: 19%). The RSD for SPM are higher ($< 32\%$): measured
 263 concentrations were close to quantification limits due to the low mass of SPM recovered on
 264 filters.

265 Enrichment Factors (EF) are classically used to determine the contamination level of solid
 266 samples (Salma and Maenhaut, 2006; Le Pape et al., 2012; Froger et al., 2018). EFs are
 267 calculated as a comparison of the Al-normalized trace element concentration in the sample
 268 with the local background values (Equation 1).

$$269 \quad EF = \frac{\frac{X_{\text{Sample}}}{Al_{\text{Sample}}}}{\frac{X_{\text{Background}}}{Al_{\text{Background}}}} \quad (1)$$

270 with X_{Sample} and $X_{\text{Background}}$ the concentrations of the element under consideration in the sample
 271 and its geochemical background, and Al_{Sample} and $Al_{\text{Background}}$ the aluminum concentrations in
 272 the sample and in the geochemical background. Local background determined for the Orge
 273 River catchment for Sb by (Froger et al., 2018) and for the Seine River for Al, Cd, Cr, Cu, Ni,
 274 Pb and Zn by (Thévenot et al., 2007) were used to calculate the EFs. Full set of elemental
 275 concentrations and associated EFs are shown in Table SI-1.7. Details on the use and
 276 calculations of enrichment factors according to the interpretation of Sutherland (2000) are
 277 given in the supplement information section.

278 **2.4.2. Radiogenic lead isotope ratio analysis**

279 Radiogenic lead isotopic ratios ($^{206}\text{Pb}/^{207}\text{Pb}$ and $^{208}\text{Pb}/^{206}\text{Pb}$) were measured by TQ-
 280 ICP-MS in solid samples previously mineralized and diluted to obtain a Pb concentration of 2
 281 $\mu\text{g.L}^{-1}$ in solution. In order to control mass bias and/or instrument drift, an isotopic Pb reference
 282 material, NIST NBS 981, was measured every two samples. To control measurement

283 accuracy, a mineralized lake sediment reference material SL1 was measured multiple times
284 with the samples and the results were compared to the data 1.217 ± 0.008 in $^{206}\text{Pb}/^{207}\text{Pb}$ and
285 2.037 ± 0.003 in $^{208}\text{Pb}/^{206}\text{Pb}$ published by Farmer et al. (2002), our SL1 measurements are in
286 the margins of errors. The method is more detailed in Supplementary information (SI-3) and
287 the results are shown in Table SI-1.8. In this study, lead isotope ratio signature was used as
288 tracer for contaminant sources to study the nature of sediment inputs in each pond system
289 (Komárek et al., 2008) using the published isotopic signature of the potential local sources of
290 Pb (Figure SI-3.1; Table SI-1.8), *i.e.* the local urban Pb endmember, the local Pb geochemical
291 background, and the French leaded gasoline.

292 **2.4.3. Antimony isotopic composition analysis**

293 An aliquot of water samples and mineralized solutions of solid samples containing
294 50-100 ng of Sb underwent a purification step on TSP cartridges (thiol-functionalized
295 mesoporous silica powder) in order to separate Sb from the other chemical species and to
296 preconcentrate it in low-concentrated samples according to the method detailed in Ferrari et
297 al. (2021). For each batch of purification, a certified reference material (BCR 723, Table SI-
298 1.9) and a blank was included. Blanks contribution represented less than 0.8 ng de Sb (<1.6%).
299 Antimony isotopic composition of the samples were then analysed by HG-MC-ICP-MS
300 (Hydride Generation coupled to a Multi-Collector Inductive Coupled Plasma Mass
301 Spectrometer, Neptune+, Thermo Fisher Scientific) on the AETE-ISO platform (OSU OREME,
302 University of Montpellier), using instrument parameter settings given in Ferrari et al. (2021). A
303 sample-standard bracketing approach was used to correct the mass bias. An in-house isotopic
304 Sb standard solution (SPEX CertiPrep (Sb $1,000 \mu\text{g mL}^{-1}$ in 20% w/w HCl, batch number 24-
305 175SBX)) was analysed before and after every sample. The isotopic composition of Sb was
306 expressed according to equation 2 which represents the deviation between the isotope ratio
307 measured for the sample and the mean isotope ratio of the in-house isotopic standard (SPEX)
308 measured before and after the sample. Detailed results are presented in Table SI-1.9.

$$\delta^{123}\text{Sb}(\text{‰}) = \left(\frac{\left(\frac{^{123}\text{Sb}}{^{121}\text{Sb}} \right)_{\text{sample}} - \left(\frac{^{123}\text{Sb}}{^{121}\text{Sb}} \right)_{\text{mean std}}}{\left(\frac{^{123}\text{Sb}}{^{121}\text{Sb}} \right)_{\text{mean std}}} \right) \times 1000 \quad (2)$$

Antimony isotopes could help in determining the transfer pathways of Sb contamination by tracing the contributions of distinct sources (Rouxel et al., 2003). Sb isotopes data have mainly been determined in mine-affected environments and river waters ($\delta^{123}\text{Sb} = -0.06\text{‰}$ to $+0.83\text{‰}$) (Resongles et al., 2015a), in environmental references samples (Rouxel et al., 2003; Ferrari et al., 2021; Sun et al., 2021; Wang et al., 2021), and in ancient glass materials (Lobo et al., 2013; Degryse et al., 2015; Dillis et al., 2019). Here, this tool is applied for the first time to road- affected surface environmental samples in an attempt to trace the contributions of distinct Sb sources, which could help in determining the transfer pathways of Sb contamination.

2.4.4. Powder X-ray diffraction (XRD)

Powder XRD diffractograms were collected on a Panalytical™ Xpert pro® diffractometer in the Bragg-Brentano geometry using Co $K\alpha$ radiation to minimize Fe X-ray fluorescence. Samples were previously crushed in an agate mortar to obtain a fine powder. Bragg reflexions were indexed using the Highscore Plus® software associated to the PDF 2 database (2020). To check for potential sample oxidation, test samples were first measured within an anaerobic chamber and results were compared to those obtained without the chamber. As no changes were observed in XRD data for underwater anoxic test samples, the whole set of samples was consequently analysed under oxic conditions. Reference compounds of ferrihydrite co-precipitated with Sb(V) or Sb(III), synthesized for X-Ray absorption measurements at the Sb K -edge (see supplementary information SI-2 for synthesis details), were analysed by X-Ray diffraction and Wide angle X-ray Scattering associated to Pair distribution function analysis on the CRISTAL beamline at SOLEIL.

331 **2.4.5. Scanning electron microscopy coupled with energy dispersive X-** 332 **ray spectroscopy (SEM-EDXS)**

333 SEM investigation associated to punctual EDXS analysis was performed on non-
334 crushed samples embedded in resin to conserve the aggregate structure of particles at the
335 microscopic scale. SEM-EDXS analyses were performed at IMPMC, with a GEMINI ZEISS™
336 Ultra55 Field Emission Gun Scanning Electron Microscope equipped with a Bruker™ Si-drift
337 detector for EDXS acquisition. Prior to analysis, bulk samples were embedded in an epoxy
338 resin (Epoxy, Presi™) and polished. Polished sections samples were coated with carbon
339 before SEM observation. EDXS spectra were performed on specific spots on the surface on
340 samples using the esprit 1.9 or 2.2 software.

341 **2.4.6. X-ray absorption spectroscopy at the Sb K-edge**

342 To examine the potential changes of Sb chemical forms along the road-to-pond
343 continuum, X-Ray Absorption Spectroscopy Near Edge Structure (XANES) measurements
344 were performed on the solid samples. Given the large shifts in energy between different types
345 of molecular environments and ligands at the Sb *K*-edge (typically 4 eV between maxima for
346 Sb(V)-O and Sb(III)-O, and 2 eV between maxima for Sb(III)-O and Sb(III)-S), XANES
347 measurements classically allow the quantification of the different species in samples of
348 unknown speciation, namely the contributions of Sb(V)-O, Sb(III)-O, and Sb(III)-S (Bennett et
349 al., 2017; Arsic et al., 2018; Burton et al., 2020). Hereafter in the text, in the section concerning
350 speciation by XANES at the Sb *K*-edge, the samples are labelled as “Dry” when they were
351 sampled as dried powders on the field and as “Underwater” when they were collected under a
352 column of water and kept under anoxic conditions until analysis. The single “Wet” sample was
353 collected as wet and dried at the laboratory under oxic conditions.

354 **2.4.6.1. Synthesis of reference compounds, sample preparation and data** 355 **sampling**

356 Ferrihydrite coprecipitated with Sb(III) and Sb(V) (Fh-Sb(III) or Fh-Sb(V)), tripuhyite
357 (FeSbO₄) and amorphous antimony trisulphide (Sb₂S₃) were synthesized to serve as reference

358 compounds. Details on the synthesis protocols can be found in the supplement information
359 section (SI-2). Sb_2O_3 was purchased from Sigma Aldrich. For reference compounds, an
360 appropriate amount of sample was diluted into cellulose and pressed in pellets for transmission
361 measurement when possible. For Fh-Sb samples, spectra were measured in fluorescence
362 mode. For environmental samples from stormwater ponds, pure sample pellets were prepared
363 by pressing approximately 50 mg of finely ground sample in a Jacomex™ glove box ($\text{O}_2 < 4$
364 ppm). All pellets were covered with Kapton® tape and transported to the synchrotron facility in
365 anoxic containers according to proven protocols (e.g. Le Pape et al., 2017).

366 Antimony *K*-edge X-ray absorption spectroscopy data were collected in both
367 transmission and fluorescence detection modes at 80 K in a liquid azote cryostat on the
368 bending magnet SAMBA beamline at SOLEIL Synchrotron (Gif-sur-Yvette, France).
369 Fluorescence signals were measured using a Canberra™ 36-elements Ge array detector and
370 incoming beam energy was monitored through a Si (220) double-crystal monochromator. Data
371 were calibrated using a Sb foil at 30,491 eV at the first inflexion point of the first derivative of
372 the XANES spectrum. Samples were mounted on PEEK sample holders in a Jacomex™ glove
373 box onsite. Sample holders were immersed in liquid N_2 for the transfer to the beamline cryostat.
374 Because Sb concentrations in samples were less than 100 mg.kg^{-1} , a minimum of 25 quick
375 scans were necessary to obtain a good signal to noise ratio for each natural sample.

376 **2.4.6.2. Data processing and analysis**

377 The FASTOSH program (Landrot, 2018) was used to calibrate and normalize Sb *K*-
378 edge extended X-Ray absorption near edge structure data and to proceed to background
379 subtraction. A linear combination fitting (LCF) analysis was performed on the XANES spectra
380 on the first derivative of the absorption to determine the relative contributions of Sb(V)-O,
381 Sb(III)-O and Sb(III)-S species in the stormwater pond samples. To do so, the Fh-Sb(V), Fh-
382 Sb(III), and am- Sb_2S_3 references compounds were considered as the most relevant to perform
383 the LCF analysis. LCF accuracy on derivative of XANES spectra were estimated by a R-factor
384 (Equation 3) and reduced chi-square (Equation 4):

385

$$386 \quad R - factor = \frac{\sum_{p=1}^t [data(p) - fit(p)]^2}{\sum_{i=1}^m [data(p)]^2} \quad (3)$$

$$387 \quad \chi_R^2 = \frac{1}{(t-s)} \sum_{i=1}^t [data(i) - fit(i)]^2 \quad (4)$$

388

389 With “data” designating the experimental spectrum, “fit” the spectrum reconstructed by LCF,
 390 “p” a specific point in each spectrum, “t” the total number of points in each spectrum, “i” an
 391 independent data point corresponding to a specific independent measurement and “s” the
 392 number of reference spectra considered in fit.

393 **3. Results**

394 **3.1. Radiogenic lead isotope ratios in solid samples**

395 The detailed results of lead isotope ratio analysis are shown in the Supplementary
 396 information (SI-3). The recent rural stormwater pond system (RR) signatures are distributed
 397 on a mixing line between the leaded gasoline and the local geochemical background
 398 endmembers. Lead isotope ratios measured in the SUR and SUO pond system fall on the
 399 same mixing line but the range of variations is smaller and isotopic signatures are close to the
 400 urban lead endmember. Extreme value close to the gasoline endmember is measured for the
 401 S-DBSI-1A10 sample collected at the entry pond spillway, *i.e.* located directly at the entrance
 402 of the pond system receiving road runoff. The closest value to the geochemical background
 403 signature is observed for the sediment sample S-P-118, which is located in SUR system
 404 natural freshwater pool receiving water from the overlaying Fontainebleau sand aquifer.
 405 Accordingly, this sample presents a particularly low Pb concentration (16 mg.kg^{-1}), confirming
 406 that this part of the system is not collecting road traffic runoff.

407

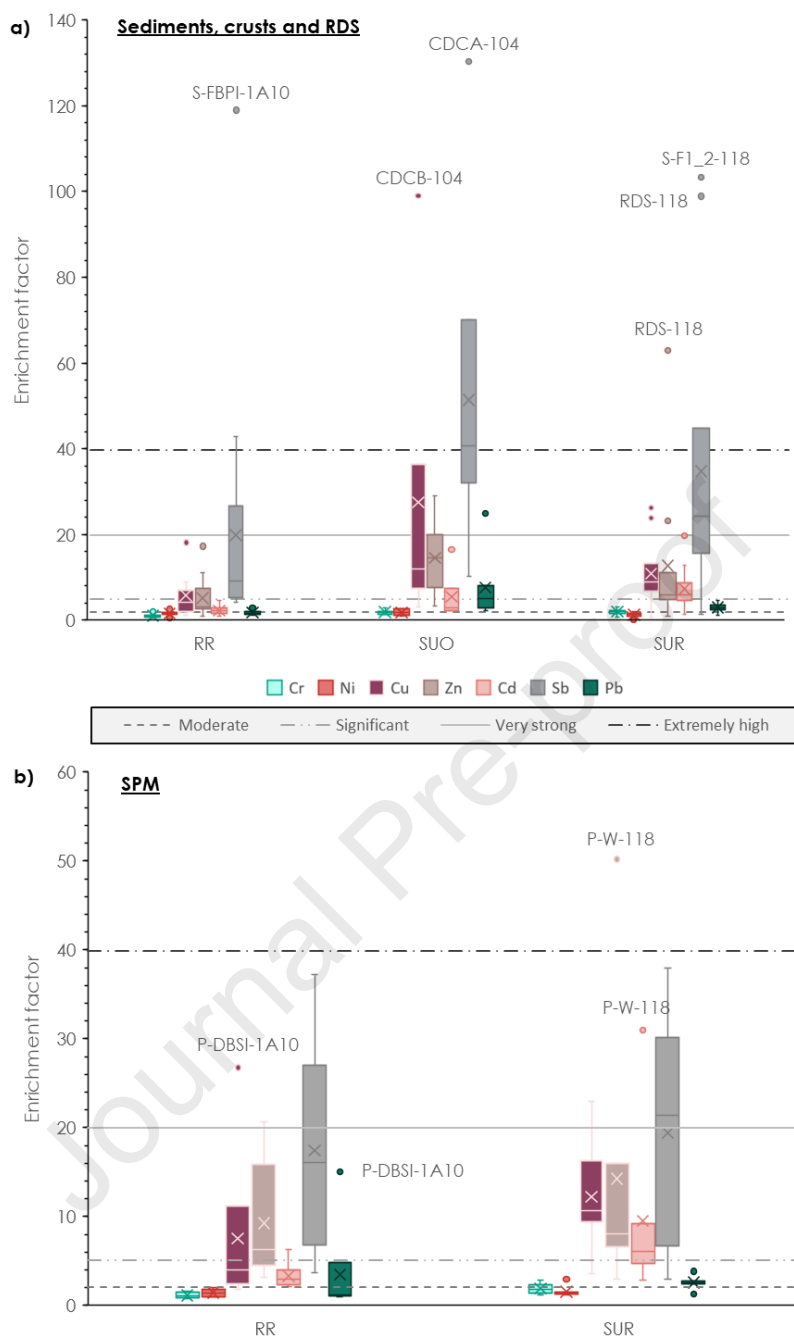
3.2. Analysis of highway stormwater pond contamination: spatial variation of elemental geochemistry and enrichment factors

Dissolved Sb concentrations (Table SI-1.5) in SUR pond system range from 0.26 $\mu\text{g.L}^{-1}$ (W-P-118) to 12.5 $\mu\text{g.L}^{-1}$ (W-W-118) in the SUR system and from 0.27 $\mu\text{g.L}^{-1}$ (W-DBFP-2A10) to 13.2 $\mu\text{g.L}^{-1}$ (W-DBSI-1A10) in the RR pond system. The only water sample available in the SUO system shows a concentration of 0.90 $\mu\text{g.L}^{-1}$ (W-DBFP-2A10).

Concentrations of trace elements in sediments, RDS and crusts samples range between 9.8 - 103 mg.kg^{-1} , <3.5 - 48 mg.kg^{-1} , 8.5-895 mg.kg^{-1} , 40 - 2539 mg.kg^{-1} , 0.2 - 3.2 mg.kg^{-1} , 0.5 - 93 mg.kg^{-1} and 8.2 - 444 mg.kg^{-1} for Cr, Ni, Cu, Zn, Cd, Sb and Pb respectively (Table SI-1.3). The corresponding EFs calculated in sediments, RDS and crusts samples are shown in Figure 2a. In the RR system, Co, Cr, Ni, Cd and Pb are not specifically enriched ($\text{EF} \leq 5$). However, EF of Cu and Zn indicate a significant contamination level ($1 \leq \text{EF} \leq 19$). In the SUO system, mean enrichment contamination level of Co, Cr and Ni are not significant ($\text{EF} \leq 3$). Zinc, Cd and Pb enrichment contamination level is classified as "significantly enriched" ($2 \leq \text{EF} \leq 29$) and Cu enrichment contamination level is very strongly enriched (EF up to 99). In SUR system, Cu enrichment contamination level reach very strong values (up to 26) and extreme values are occasionally observed for Zn (EF = 63 in RDS-118). In the three studied stormwater pond systems, Sb is extremely enriched with respect to the local geochemical background, with maxima EF values as high as 119 in RR (S-FBPI-1A10), 130 in SUO (CDCA-104) and 103 (S-F1_2-118) in SUR system, attesting of important inputs of Sb in this urban area. It is noteworthy that the Sb natural abundance is low, with a local geochemical background of 0.2 - 0.5 mg.kg^{-1} (Froger et al., 2018). Therefore, the Sb geochemical anomaly induced by anthropogenic Sb emissions in this urban context is particularly prominent (as reflected by extreme EF values), this trend has already been observed in other large cities (Chen et al., 2008; Gonzales et al., 2016; Dong et al., 2017; Nory et al., 2021).

In comparison with sediments, SPM is a dynamic component in this type of system. Metal concentrations (Table SI-1.4) and EFs (Figure 2b) in SPM have been quantified to give

435 a picture of contamination transfer by surface particles. Concentrations of trace elements in
436 SPM samples range between 44 - 186 mg.kg⁻¹, 18 - 57 mg.kg⁻¹, 51 - 985 mg.kg⁻¹, 168 - 5019
437 mg.kg⁻¹, 0.6 - 10 mg.kg⁻¹, 2 - 83 mg.kg⁻¹ and 24 - 738 mg.kg⁻¹ for Cr, Ni, Cu, Zn, Cd, Sb and Pb
438 respectively. As observed for sediments, Co, Cr and Ni are not particularly enriched in RR and
439 SUR systems (Figure 2b). In contrast, Cu, Zn and Sb are significantly enriched in RR and SUR
440 systems. Cadmium is also significantly enriched in SUR system while only moderately
441 enriched in RR system sediments. Lead is moderately enriched in RR and SUR systems
442 sediments. Again, Sb presents the highest mean EF in SPM in both RR and SUR systems
443 sediments. Otherwise, two punctual very strong EF values are observed in the RR system for
444 the sample P-DBSI-1A10 at 27 for Cu and 21 for Zn. In the SUR system, extreme values are
445 determined for the sample P-W-118 at 50 for Zn and 31 for Cd. EF determined in SPM of the
446 RR and SUR systems are comparable between both ponds while their EF are different in
447 sediments.



448

449 **Figure 2.** Aluminium-normalized enrichment factors for a) sediments, soil, RDS and crusts and
 450 b) SPM samples compared to the local geochemical background (Thévenot et al., 2007; Froger
 451 et al., 2018). Chromium EF are shown in cyan, Ni in red, Cu in purple, Zn in taupe, Cd in pink,
 452 Sb in grey and Pb in green. Eighteen samples are considered for constructing the box plot in
 453 the RR system, 7 for SUO system, 10 for SUR system. Six samples are considered for SPM
 454 in RR system and 7 in SUR system. The bottom branch of each boxes represents the minimum
 455 value, the bottom of the box represents the first quartile, the horizontal line inside the box
 456 represents the median value, the cross represents the mean value, the top of the box
 457 represents the third quartile, the dots represent extreme values and the top of the branch
 458 represents the maximum value for series without extreme values. Horizontal lines indicate the
 459 level of enrichment according to the classification of Sutherland, (2000).

460
461 The Cu/Sb ratio is frequently used in literature to trace the brake pad contamination in
462 areas impacted by road traffic (e.g. Stechmann and Dannecker, 1990). Indeed, these two
463 elements are important constituents of brake pads (Dong et al., 2017). In our study, the local
464 geochemical background can be estimated at Cu/Sb = 25 (Sb concentration from Froger et al.
465 (2018) and Cu from Thévenot et al. (2017)). In the SUR system, Cu/Sb reach up to 39 in S-W-
466 118 (natural pond) and down to 6 in RDS-118, with an average of 12 and 9 if the two samples
467 from natural pond are excluded (S-W-118 and S-P-118). SUO system Cu/Sb values are
468 between 6 (RDSB-104) and 35 (CDCB-104) with an average of 12. In RR system the Cu/Sb
469 values are situated between 4 (S-FBPI-1A10) and 21 (CD2-1A10) with an average of 9.

470 3.3. Analysis of Sb sources using $\delta^{123}\text{Sb}$ isotopic signatures

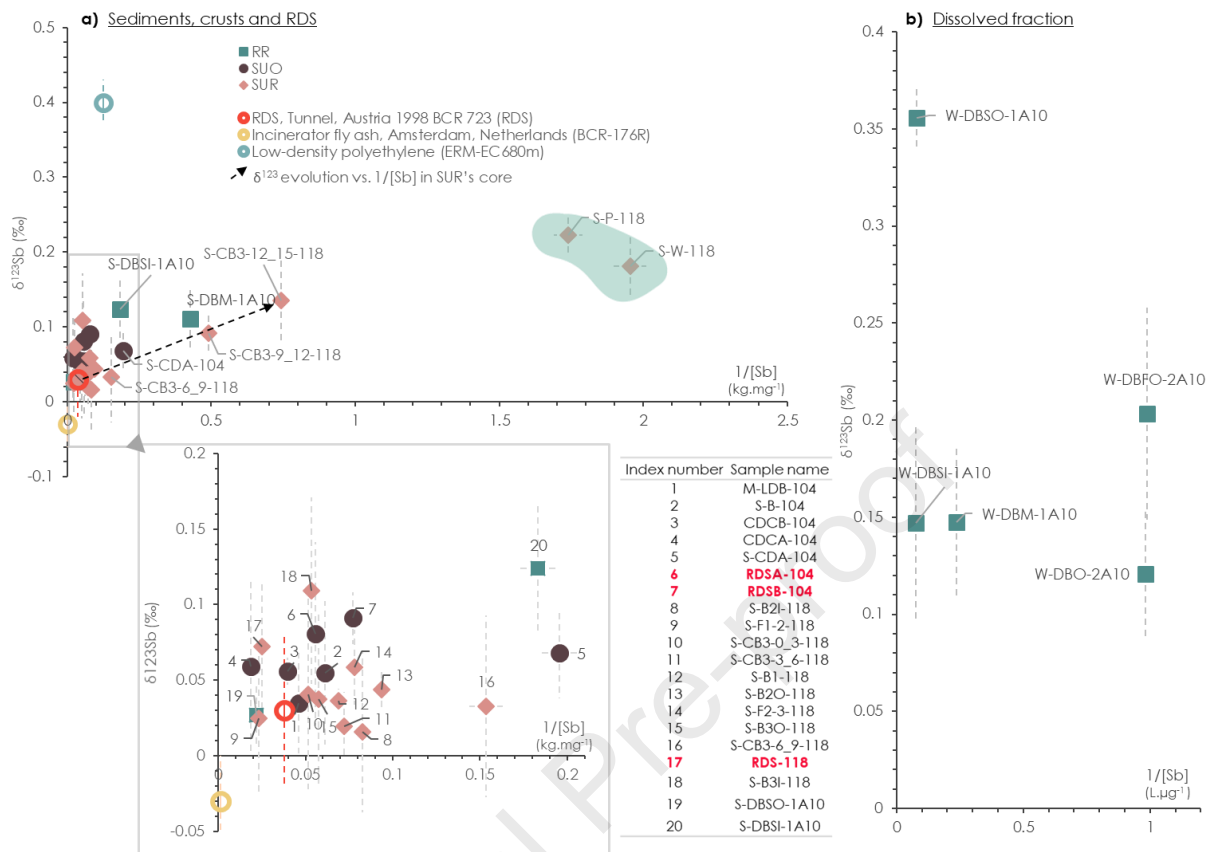
471 Antimony isotopes are applied for the first time to road- affected surface environmental
472 samples in an attempt to trace the contributions of distinct Sb sources, which could help in
473 determining the transfer pathways of Sb contamination. Figure 3a and 3b present $\delta^{123}\text{Sb}$
474 values as a function of $1/[\text{Sb}]$ for solid and liquid samples, respectively. Antimony isotopic
475 compositions of solid samples measured at the three sampling sites range from $0.02 \pm 0.02\text{‰}$
476 to $0.22 \pm 0.03\text{‰}$ with an average of $0.07 \pm 0.05\text{‰}$ ($n=25$). No significant variation of the average
477 $\delta^{123}\text{Sb}$ values was observed between the sampling sites ($\delta^{123}\text{Sb}_{\text{SUO}} = 0.06 \pm 0.02\text{‰}$ ($n=7$);
478 $\delta^{123}\text{Sb}_{\text{SUR}} = 0.06 \pm 0.04\text{‰}$ ($n=13$), excluding the two samples of the natural pond); $\delta^{123}\text{Sb}_{\text{RR}} =$
479 $0.09 \pm 0.05\text{‰}$ ($n=3$)). On average, values observed for the sediments are closer from those
480 reported by Ferrari et al. (2021) for the certified reference material of Austrian RDS (BCR 723,
481 $\delta^{123}\text{Sb} = 0.03 \pm 0.05\text{‰}$) than from both Netherlands incinerator fly ash (BCR 176R, $\delta^{123}\text{Sb} =$
482 $0.03 \pm 0.03\text{‰}$) and low-density polyethylene (ERM-EC 680m, $\delta^{123}\text{Sb} = 0.40 \pm 0.03\text{‰}$). Taken
483 individually, road deposit sediment (RDS) samples from the SUO and SUR pond systems,
484 represented in red on the zoom part of Figure 3a, present $\delta^{123}\text{Sb}$ values and $1/[\text{Sb}]$ values
485 relatively close from those of the BCR 723 (Austrian RDS collected in an urban tunnel), with

486 $\delta^{123}\text{Sb} = 0.07 \pm 0.04\text{‰}$ for RDS-118, $0.08 \pm 0.06\text{‰}$ for RDSA-104 and $0.09 \pm 0.02\text{‰}$ for RDSB-
487 104.

488 Two samples of the SUR system highlighted in green in Figure 3a present the highest
489 $\delta^{123}\text{Sb}$ values ($0.18 \pm 0.04\text{‰}$ for S-W-118 and $\delta^{123}\text{Sb} = 0.22 \pm 0.03\text{‰}$ for S-P-118), associated
490 with low Sb concentrations close to the geochemical background (0.51 mg.kg^{-1} and 0.57
491 mg.kg^{-1}). These samples are interpreted as not directly impacted by road emission, which is
492 consistent with lead isotope ratio data (see SI-3). In SUR system, five sediment samples taken
493 in a 15 cm core sampled every 3 cm in the B3 SUR basin (Fig. 1) show a decreasing
494 concentration in Sb as a function of depth in the core (19.4 mg.kg^{-1} for S-CB3-0_3-118 and
495 1.35 mg.kg^{-1} for S-CB3-12_15-118) with a concomitant slight increase of $\delta^{123}\text{Sb}$ values from
496 $0.02 \pm 0.02\text{‰}$ to $0.04 \pm 0.06\text{‰}$ for 0 - 9 cm depth and from $0.09 \pm 0.02\text{‰}$ to $0.13 \pm 0.06\text{‰}$ for
497 9 - 15 cm depth.

498 For water samples from the RR system, $\delta^{123}\text{Sb}$ ranges from $0.12 \pm 0.03\text{‰}$ to $0.36 \pm$
499 0.02‰ with an average of $0.19 \pm 0.09\text{‰}$ ($n=5$). Thus, dissolved Sb presents an enrichment in
500 heavy Sb isotope compared to particulate Sb (average $\delta^{123}\text{Sb}_{\text{RR}} = 0.09 \pm 0.05\text{‰}$, $n=3$) at this
501 RR pond site. Interestingly, at the DBSO sampling point, corresponding to a spillway
502 separating the settling and filtration ponds, a strong difference between the $\delta^{123}\text{Sb}$ signatures
503 of the sediments and the dissolved phase is observed: $0.03 \pm 0.02\text{‰}$ and $0.36 \pm 0.02\text{‰}$,
504 respectively. This indicate a significant fractionation of Sb isotopes between the dissolved and
505 solid phases at this particular spot where reducing conditions were observed.

506



507

508 **Figure 3.** $\delta^{123}\text{Sb}$ as a function of $1/[\text{Sb}]$ (Sb concentration in mg.kg⁻¹ or L.μg⁻¹) given for (a)
 509 sediments, crusts, RDS and (b) water samples (dissolved fraction). Samples from SUR system
 510 are represented as pink diamonds; sediments, soils, crusts and RDS from SUO system
 511 are represented as dark purple dots; sediments from RR system are represented as blue filled
 512 squares and waters as blue contoured squares. $\delta^{123}\text{Sb}$ values from certified reference material
 513 published by Ferrari et al. 2021 are also represented: tunnel RDS (BCR 723) in red circle,
 514 incinerator fly ash (BCR -176R) in yellow circle and low-density polyethylene (ERM-EC 680m)
 515 in blue circle. The supposed local natural signatures are circled by a light blue area and
 516 samples from a core situating along the black dotted arrow. RDS sample labels are represented
 517 in red in the zoom figure and in the associated table. $\delta^{123}\text{Sb}$ data and Sb concentrations are
 518 available in Table SI-1.9 in Tables SI-1.3 and SI-1.5, respectively.

519

520 3.4. Antimony mineralogy and speciation as studied at the particle and

521 molecular scales

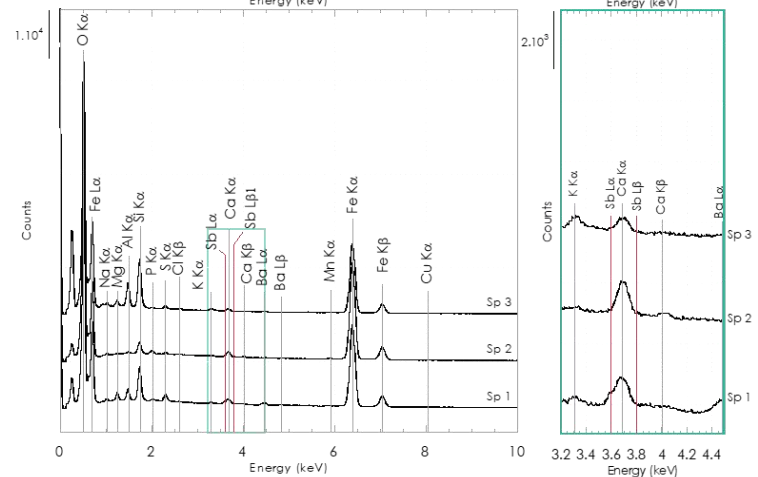
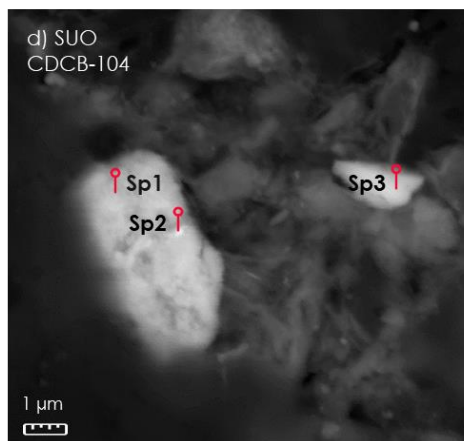
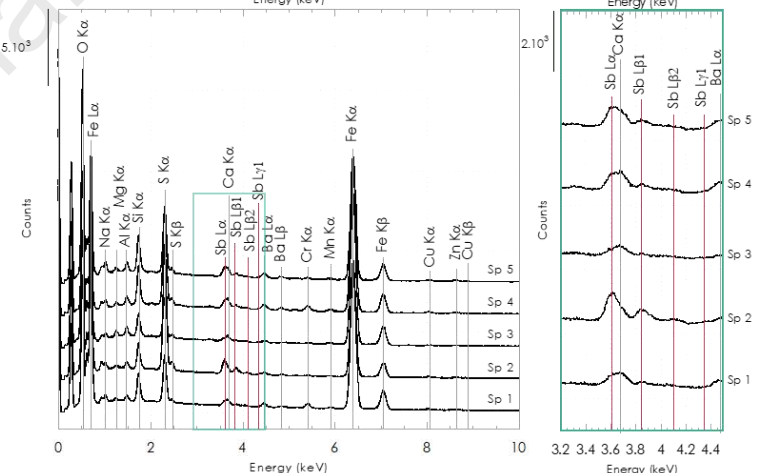
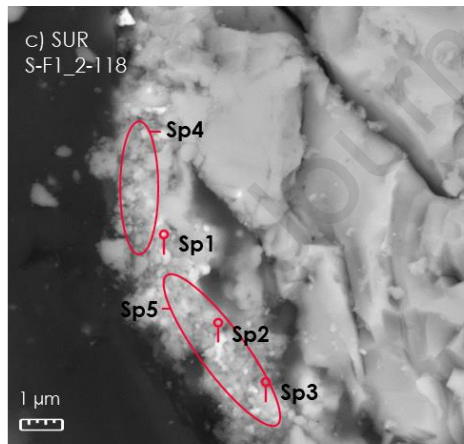
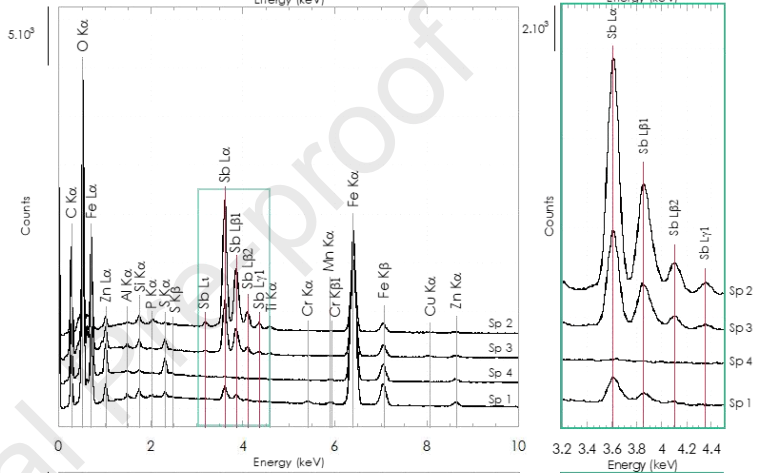
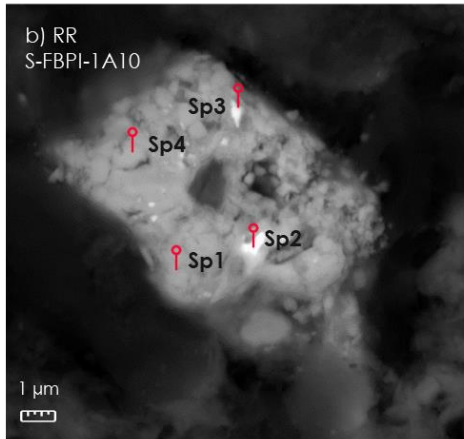
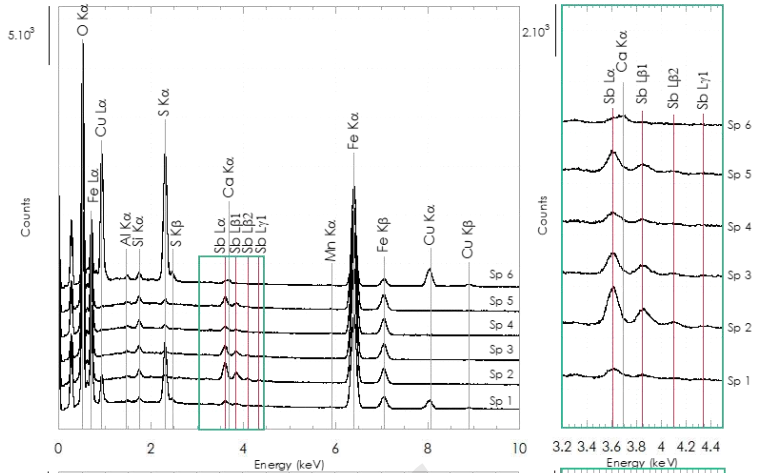
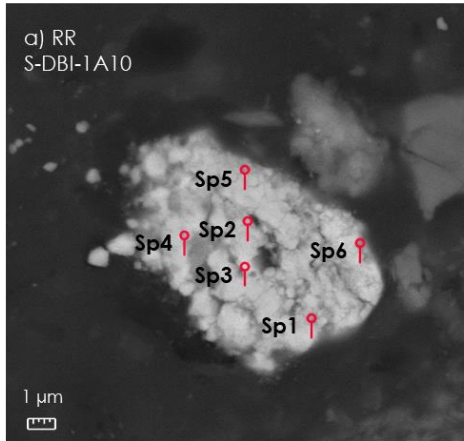
522 To study the mineralogy of solid samples in the stormwater ponds, we have performed
 523 powder XRD measurements (Fig. SI-1.4). The main mineralogical components (>1%wt) are
 524 usual geogenic surface minerals such as quartz, calcite and feldspars. At low diffraction angle,

525 the presence of different types of phyllosilicates such as chlorite, illite and kaolinite is observed
526 on the basis of the (001) reflexions, and small amounts of additional dolomite were observed
527 in the SUR system samples. For some samples, a weak reflexion around 8.4 Å indicates the
528 presence of amphibole-type minerals.

529 A systematic SEM-EDXS study was carried out on the samples with the objectives of
530 (1) documenting the mineralogy of these Sb-enriched samples constituted of both natural and
531 road derived materials at the aggregate scale, and (2) uncovering discrete Sb-bearing
532 phase(s) (Fig. 4). Depending on the input of local geogenic particles in the samples, mineral
533 aggregates of varying sizes ($>2\ \mu\text{m}$) (Fig. SI-1.5) were observed. In particular, in RDS samples,
534 we observed metallic spherules possibly resulting from abrasion of car/road materials (Fig. SI-
535 1.7). In general, in all samples, particles made of metallic alloys were observed, e.g. particles
536 containing Ti, Cr, Cd, Zn and rare earth elements (REE) (Fig. SI-1.6). An important contribution
537 of iron oxyhydroxides/oxides was also observed. Antimony was detected in particles in the
538 three pond systems *via* punctual EDXS analysis using the *L*-emission lines as diagnostic
539 spectral pattern ($L\alpha_1$ 3,604.72 eV, $L\alpha_2$ 3,595.32 eV, $L\beta_1$ 3,843.57 eV, $L\beta_2$ 4,100.78 eV, $L\gamma_1$
540 4,347.79 eV and $L\gamma_2$ 3,192 eV). In the RR samples S-DBI-1A10 (Fig. 4a) and S-FBPI-1A10 (Fig.
541 4b), the analysed Sb-bearing particles showed different chemical compositions depending on
542 the spot where the analysis was performed. Indeed, the presence of Sb is always concomitant
543 with the one of Fe, while Sp1 and Sp6 spots (Fig. 4a) qualitatively show the additional presence
544 of S, Cu and Na. The sample S-FBPI-1A10 (Fig. 4b) shows the presence of Zn and particularly
545 high level of Sb at discrete submicrometric spots, especially in Sp2 where Sb content is
546 qualitatively higher than Fe. In the sample S-F1_2-118 from the SUR system (Fig. 4c), Sb was
547 also found as submicrometric particles associated with Fe oxyhydroxides/oxides. In S-F1_2-
548 118, punctual EDXS spectra (Sp1, Sp2 and Sp3) and EDXS spectra of areas (Sp4 and Sp5)
549 show roughly the same amount of S, Fe and Cu, but Cr and Ba are also detected. Sp2
550 spectrum, taken on the spot presenting the higher backscattering intensity accordingly shows
551 the highest Sb signal compared to spectra Sp1 and Sp3. In SUO system, on sample

552 CDCB-104 (Fig. 4d), the particle containing Sb was also observed as associated with an iron-
553 containing particle (containing also major elements such as Ca). Because the Ca *K*-emission
554 line overlaps with the main *L*-emission line of Sb, the signal is more difficult to distinguish but
555 remains visible, for instance in the Sp1 spectra (Fig. 4d) in which Cu, S and Ba are also
556 detected.

Journal Pre-proof

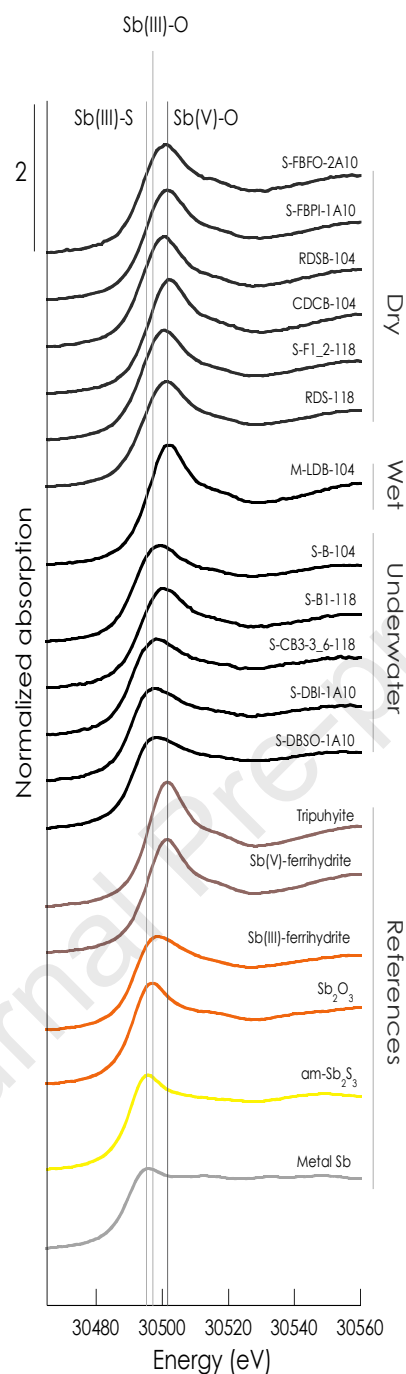


558 **Figure 4.** SEM images taken in backscattering mode (left), and qualitative EDXS analyses on
559 the right for three samples representative of each highway stormwater pond systems SUR,
560 SUO and RR. A zoom between 3.2 and 4.4 KeV on the X-Ray emission spectra (green
561 rectangle) shows the presence of Sb on the basis of the $L\alpha_1$ to Li emission lines. Sediments
562 S-DBI-1A10 (a) and dry sediment S-FBPI-1A10 (b) (RR system) are represented on the first
563 and second lines, dry sediment S-F1_2-118 (c) (SUR system) on the second line and crust
564 CDCB-104 (d) (SUO system) on the bottom line.

565

566 Calibrated and normalized XANES data include both samples from the field and
567 selected reference compounds (Fig. 5). The reference compounds selected in which Sb is
568 under the Sb(V)-O form are tripuhyite ($FeSbO_4$) and ferrihydrite co-precipitated in the presence
569 of dissolved Sb(V). The reference compounds selected in which Sb is under the Sb(III)-O form
570 are ferrihydrite co-precipitated in the presence of dissolved Sb(III) and Sb_2O_3 . Finally, the
571 chosen reference compound representative of the Sb(III)-S molecular environment is
572 amorphous Sb_2S_3 . Additionally, the metallic Sb foil was considered as a Sb(0) metal/alloy
573 reference. Qualitative examination of XANES spectra (Fig. 5) shows that the maximum of
574 absorption of the "dry" samples is shifted towards the higher energies, *i.e.* the oxidized species
575 with oxygen ligand Sb(V)-O. On the contrary, the "Underwater" samples show maxima shifted
576 towards lower absorption energies and therefore present a non-negligible contribution of
577 reduced Sb species (*e.g.* Sb(III)-O and/or Sb(III)-S).

578

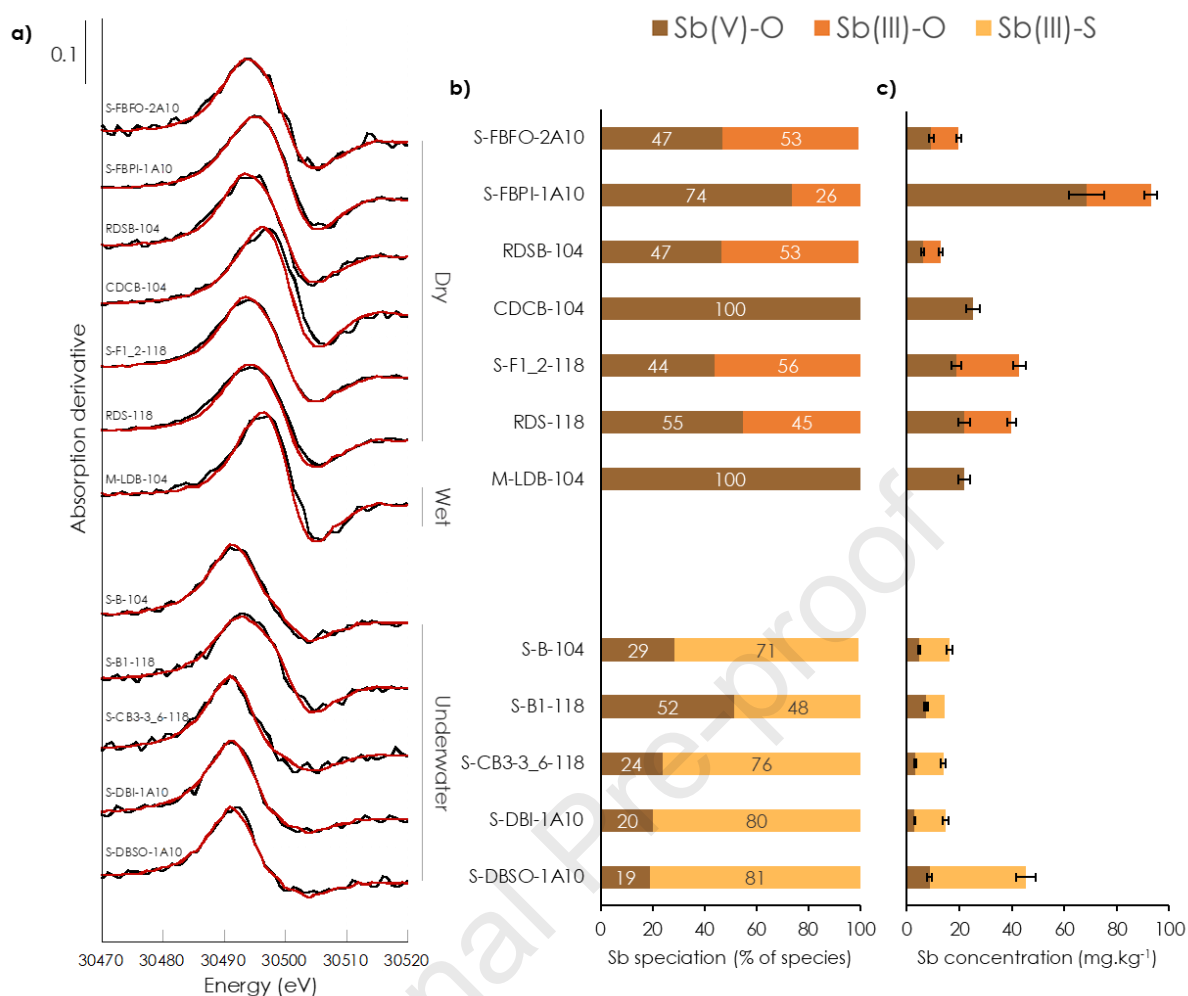


579

580 **Figure 5.** Antimony *K*-edge XANES spectra of dry and wet samples, underwater samples
 581 (black) collected in the three studied sites in the Paris region (France), Sb(V)-O references
 582 (brown) are tripuhyite (FeSbO_4) and Sb(V) co-precipitated ferrihydrite; Sb(III) references are
 583 Sb(III) co-precipitated ferrihydrite, Sb_2O_3 (orange) and amorphous Sb_2S_3 (yellow); Sb(0) is
 584 represented by metal Sb (grey). Vertical lines represent the maximum of XANES signal for
 585 known chemical environments and ligands, namely Sb(V)-O (30 501 eV), Sb(III)-O (30,497-
 586 30,499 eV), Sb(III)-S (30,496 eV), and Sb(0) (=Sb-Sb, 30,496 eV).

587

588 To quantify the contribution of different oxidation states and ligands in Sb speciation,
589 we proceeded to a LCF analysis on the derivative of the Sb *K*-edge XANES spectra using
590 three reference samples representative of the system geochemistry, namely Sb(V)-ferrihydrite
591 (Sb(V)-O), Sb(III)-ferrihydrite (Sb(III)-O), and amorphous Sb₂S₃ (Sb(III)-S). Results of LCF are
592 presented on Figure 6 and in Table SI-1.10. In the “dry” samples, the Sb(V)-O form dominates
593 although the Sb(III)-O species are present in significant proportions, between 26% and 56%,
594 except in CDCB-104 in which only the Sb(V)-O form is detected. Likewise, the “wet” sample
595 M-LDB-104 contains only Sb(V)-O species. In contrast, in the “underwater” samples, Sb
596 speciation is dominated by the Sb(III)-S species (from 48% to 81%). Figure 6c presents Sb
597 speciation normalized to total Sb concentrations in the samples. Thus, we observe that
598 “underwater” samples presenting the main Sb(III)-S signature are likely less concentrated in
599 Sb, between 13.9 mg.kg⁻¹ for S-CB3-3_6-118 to 45.3 mg.kg⁻¹ for S-DBSO-1A10 than “dry”
600 samples presenting concentrations up to 93 mg.kg⁻¹ in the S-FBPI-1A10 sample (Fig. 6c).



601

602 **Figure 6.** (a) Results of the linear combination fitting procedure applied on the absorption first
 603 derivative of XANES spectra (experimental data in black and fit in red). (b) Proportion of
 604 Sb(V)-O species (brown), Sb(III)-O species (orange) and Sb(III)-S species (yellow) normalized
 605 to 100% (more details of the species in supplementary information). (c) Results of LCF
 606 normalized (%) to total Sb concentration (mg.kg⁻¹) in the samples. Errors on components
 607 determined by LCF are considered to be 10%.

608

609 4. Discussion

610 4.1. Geochemical parameters as tracers of emission sources in near-road 611 environments

612 Radiogenic Pb isotope ratios validate the 2 categories established by the land-use
 613 observed in the drained area of the systems: semi-urban (SUO and SUR) and rural systems
 614 (RR), on the basis of our knowledge of Pb isotopic endmembers in urban areas. Moreover,
 615 heterogeneous isotopic signatures observed and the close to former lead gasoline signatures

616 in 2 samples of the RR system show that Pb isotopes cannot be directly used to infer the age
617 of highway stormwater ponds (see SI-2). Indeed, former lead gasoline signature has been
618 shown to still contributed to impact urban environments (Ayrault et al., 2012; Resongles et al.,
619 2021).

620 Enrichment factors ranging between 0.4 and 130 are observed for Co, Cr, Ni, Cu, Zn, Cd, Sb
621 and Pb. They are of the same magnitude with those previously observed in near road
622 environments (Meland et al., 2010). Different sources for these metals are evoked in the
623 literature, among which abrasion of brake linings for Cu, Sb, Zn, Pb, Cr and, to a lesser extent,
624 of Ni and Cd (Sörme and Lagerkvist, 2002; Hjortenkrans et al., 2007; Thorpe and Harrison,
625 2008). Zinc, which is strongly enriched in our system, is also used in tires and motorway crash
626 barriers (Sörme and Lagerkvist, 2002; Zhang et al., 2004; Hjortenkrans et al., 2007). Cobalt,
627 Zn, Pb, Cr, Ni and Cd, as constituents of car bodies, can be released to the environment by
628 simple rain leaching (Störm and Lagerkvist, 2002), probably explaining a part of the emissions
629 given the high flux of vehicles on the road investigated (Table 1). In this study, enrichments in
630 Cd, Cr and Ni are found to be more limited in sediments and SPM in comparison with the data
631 of Hjortenkrans et al. (2007) in road environments. Here, the higher enrichment factors of Pb
632 in semi-urban systems sediments compared to the rural system is in line with the results of Pb
633 isotopic signatures that indicate a major urban source contribution. Cadmium and Cr,
634 presenting higher concentrations in the SUR system compared to RR and SUO systems, (Fig.
635 SI-1.2) might have a different or an additional source at SUR compared to RR and SUO (Fig.
636 2). Both Cr and Cd enrichments occurred in the third basin (B3, SUR system), also connected
637 to the natural pond (Fig. 1), itself hydrologically connected to the overlying Fontainebleau sand
638 aquifer. We thus hypothesize that Cd and Cr could have been emitted by past industrial/urban
639 activities (Avino et al., 2008; Byrne et al., 2017) on the Plateau of Saclay situated upstream or
640 by a geogenic source from the Fontainebleau sands aquifer (which geochemistry is not yet
641 documented). Correlations of Sb with Cu concentrations in the solid phase (Fig. SI-1.2) point
642 to a potential common source such as emission from brake pads (Thorpe and Harrison, 2008).

643 If the ratio Cu/Sb is constant in the road environment, and different from that of the
644 geochemical background, it is then possible to determine the anthropogenic contribution in the
645 environment studied. Figure SI-1.8 represents Cu/Sb ratios of the collected solid samples as
646 compared to the Cu/Sb ratios listed in the literature. In the literature, brake pads Cu/Sb is 16.5
647 on average with variations from 3.5 to 29 (Weckwerth, 2001; Hjortenkrans et al., 2007; Dong
648 et al., 2017). In Sweden, this high range of observed values was explained by the occurrence
649 of different brake suppliers. In the study of Hjortenkrans et al. (2006) focusing on PM₁₀, Cu/Sb
650 are between 4.9 and 15.1 with a median of 5.5. Top soils collected at less than 0.5 m from the
651 road pavement show mean Cu/Sb of 20 (Hjortenkrans et al., 2006) and Cu/Sb ratio of 28 was
652 measured in RDS (Dong et al., 2017). Here, the RDS samples show low Cu/Sb values, ($6 \leq$
653 $\text{Cu/Sb} \leq 7$). Excluding the SUR natural pond ($\text{Cu/Sb} \geq 14.8$), the underwater sediments show
654 Cu/Sb values between 5.2 and 10.7, which is well below the values determined for the local
655 geochemical background ($\text{Cu/Sb} = 25$). A possible source of variation could be that Sb and Cu
656 could also be emitted by oil leakages containing anti-frictions materials such as tin-based
657 babbitt alloys used as dry lubricants in engine bearings in case of oil pump failure, themselves
658 presenting various compositions (Paleu et al., 2016).

659 Zinc concentrations in solid samples are positively correlated with Sb concentrations (Fig. SI-
660 1.2, R^2 of 0.92 and 0.73 for RR and SUO respectively, and 0.65 for SUR (0.99 excluding RDS-
661 118)), also pointing to a possible common source in road environments. In the SUR system,
662 the RDS sample (RDS-118) might contain a fraction of galvanized steel issued from the
663 sampled surface, explaining its high Zn concentration. As the Zn-Sb correlation is observed
664 both in urban and rural environments, the source of emission is likely due to abrasion of
665 vehicles constituents, including brake pads (Hjortenkrans et al., 2007).

666

667 **4.2. Antimony elemental and isotopic geochemistry and associated sources**

668 Antimony concentrations in dissolved fractions (0.26 to 13.2 $\mu\text{g.L}^{-1}$) are comparable to
669 the concentrations measured in a stormwater pond in Oxford (0.67 - 8.19 $\mu\text{g.L}^{-1}$,

670 Kamalakkannan et al., 2004). These values are higher than the ones observed in the Orge
671 River even in the highly urbanized areas ($0.23\text{-}0.44\ \mu\text{g.L}^{-1}$ at Viry-Châtillon, Le Pape et al.,
672 2012). In the SUR natural pond not impacted by traffic runoff, the high dissolved concentration
673 of Sb ($12.5\ \mu\text{g.L}^{-1}$) does not reflect the concentrations in the corresponding sediment (0.5
674 mg.kg^{-1}) and SPM ($6.1\ \text{mg.kg}^{-1}$) fractions. Explaining this particular enrichment in dissolved Sb
675 would need further research to determine if it was a punctual anomaly (e.g. local contamination
676 of the overlying aquifer) or a permanent input from the Fontainebleau sand aquifer waters. Our
677 values only exceptionally exceed the European guidelines for Sb concentration in drinking
678 water fixed at $10\ \mu\text{g.L}^{-1}$ (directive UE 2020/2184) and are below the drinking water guidelines
679 for antimony ($<20\ \mu\text{g.L}^{-1}$) as stated by the World Health Organization (Guidelines for Drinking
680 water quality, 2017).

681 All the solid samples collected in the ponds, including sediments, crusts and soils, present an
682 average $\delta^{123}\text{Sb}$ signature of $0.07 \pm 0.05\text{‰}$ ($n=25$), which is close to the RDS reference material
683 (BCR-723, $\delta^{123}\text{Sb}$ of 0.03‰ , Ferrari et al., 2021). Additionally, the $\delta^{123}\text{Sb}$ signatures of RDS
684 samples measured in this study (Fig. 3) are also close to the BCR-723 signature. The RDS
685 signature could then reflect a mean isotopic signature of Sb in brake pads in use in France
686 over the last decennials. The low concentrated sediment samples in the SUR natural pond (0.5
687 $\text{-}0.6\ \text{mg.kg}^{-1}$) show heavier $\delta^{123}\text{Sb}$ signatures (S-W-118 $18 \pm 0.04\text{‰}$ and S-P-118 $22 \pm 0.03\text{‰}$)
688 than most of the samples from the stormwater ponds on the same site (Fig. 3). We could thus
689 hypothesize that these samples could trace the local geochemical endmember (Fig. 3, in
690 green), or a different source resulting from the industrial activities of the Saclay plateau located
691 above. Nevertheless, the hypothesis of a local Sb contamination source different from the road
692 is less plausible considering the low concentrations and EF measured in the natural pond.
693 Moreover, $\delta^{123}\text{Sb}$ and the Sb concentration of the core samples vary slightly from the bottom
694 to the top with a heavier signature $\delta^{123}\text{Sb}$ 0.13‰ at the bottom ($1.3\ \text{mg.kg}^{-1}$) going down to
695 0.04‰ at the top sample with a higher concentration ($19\ \text{mg.kg}^{-1}$). Considering the local
696 background signature determined as $0.18\text{‰} - 0.22\text{‰}$, this variation could be explained by the

697 higher contribution of geogenic materials in deeper samples. Albeit global $\delta^{123}\text{Sb}$ signature
698 points towards a close range of values, the local variation observed on some samples could
699 putatively be ascribed to fractionation due to post-depositional processes. Indeed, in the RR-
700 2A10 pond, two samples present diverging $\delta^{123}\text{Sb}$ values in the dissolved fraction (W-DBFO-
701 2A10 and W-DBO-2A10) while having the same Sb concentration. DBFO could represent the
702 $\delta^{123}\text{Sb}$ value for input water whereas DBO could represent the equilibrated value after a longer
703 residence time in the pond. This might be due to isotope fractionation between the dissolved
704 and solid fractions in the pond due to specific biogeochemical processes
705 (reduction/oxidation/ligand exchange) occurring within the sediments, potentially attesting of
706 Sb exchanges between the solid phase and the overlying water column. In the RR-1A10 reed-
707 planted pond, particularly interesting observations are made for the samples DBSI, DBM, and
708 DBSO, located from the entrance to the exit of the settling pond, respectively. For DBSI and
709 DBM, dissolved and sediment fractions present similar $\delta^{123}\text{Sb}$ signatures (DBSI, $0.15 \pm 0.05\text{‰}$
710 dissolved vs. $0.12 \pm 0.04\text{‰}$ solid, and DBM, $0.15 \pm 0.04\text{‰}$ dissolved vs. $0.11 \pm 0.04\text{‰}$ solid)
711 whereas for DBSO they significantly differ ($0.36 \pm 0.02\text{‰}$ dissolved vs. $0.03 \pm 0.02\text{‰}$ solid).
712 We could hypothesize that this particular fractionation at the DBSO site could possibly be a
713 consequence of Sb(V) reduction to Sb(III) under anoxic conditions, and/or to ligand exchange
714 from oxygen to sulphur (Rouxel et al., 2003; Ferrari et al., 2022), which would be supported by
715 the LCF-XANES analysis on this Sb-rich ($45.3 \pm 2.7 \text{ mg.kg}^{-1}$) sample showing an important
716 contribution of reduced Sb (Sb(III)-S = $81 \pm 10\%$ vs. Sb(V)-O = $19 \pm 10\%$). A smell of sulphide
717 was also noticed at the DBSO sampling point, indicative of sulphide-producing conditions that
718 might also induce a fractionation of Sb between dissolved and solid fractions, for instance due
719 to production of thio-Sb intermediates (Ye et al., 2019). Alternatively, other physico-chemical
720 processes could play a role in Sb isotope fractionation. For instance, preferential adsorption of
721 light Sb isotope has been observed with Sb(V) on alumina due to kinetic effects, leaving
722 heavier Sb isotope in aqueous phase (Zhou et al., 2022).

SEM-EDXS allowed us to observe discrete phases carrying Sb (Fig. 4) directly pointing to the brake pad source. In the three systems Sb was similarly observed on micro-particles with high backscattering signal associated to iron oxides (Fig. 4). In these particles, Fe, S, Cu, Zn and Ba are observed in addition to Sb (Fig. 4), as it has already been observed in some brake pads (Ingo et al., 2004). Due to brake friction, the high temperature leads to the oxidation of Sb_2S_3 lubricant and oxidizes Sb_2S_3 into Sb_2O_5 , Sb_2O_3 and/or Sb_2O_4 , depending on the temperature generated by the braking process and the initial composition of brake pads (Ingo et al., 2004; Cho et al., 2006; Martinez and Echeberria, 2016). These Sb oxides would then react with metallic iron included in the brake pad to form iron oxides, metallic Sb, and/or Fe-Sb containing alloys (Matějka et al., 2011; Martinez and Echeberria, 2016). Even if its use will probably tend to decrease since health and environment safety decisions in the USA are leading to a ban of Sb in brake pads (US EPA Copper-Free Brake Initiative), these observations and the nature of phases containing Sb observed by SEM-EDXS strongly suggest that brake pads are a present-day source of Sb emission from road traffic at the sampling sites. It is important to note that Sb could also be present, even in a large extent, as associated with mineral phases at lower concentration, non-detectable with the SEM-EDXS method. To obtain an image of Sb speciation at the scale of the bulk sample, taking also into account the Sb dispersed within other mineralogical phases at trace level, we applied X-ray absorption spectroscopy at the Sb *K*-edge.

4.3. Antimony geochemical reactivity in road impacted surface

environments

Linear combination fits of XANES derivative spectra at the Sb *K*-edge show that both Sb(V)-O and Sb(III)-O are observed in solids sampled in “dry” oxic conditions (Fig. 5). In a previous study, Sb(III) and Sb(V) with both oxygen and sulphur ligands have been detected in urban road samples such as RDS and aerosols (10 μm and 2.5 μm) (Varrica et al., 2013). In this latter study, the authors interpret their speciation as a result of Sb_2S_3 -containing brake pad abrasion producing Sb oxides (Sb_2O_3 (Sb(III)-O), and Sb_2O_5 (Sb(V)-O) species) as also

750 identified by Matějka et al. (2011). Here, we confirm that, in dust directly produced by road
751 traffic, *i.e.* in the RDS sampled upstream from the studied pond systems, mixed
752 Sb(V)-O/Sb(III)-O oxidation states were present, which would also be in agreement with
753 emissions from brake pads. This tends to indicate, together with SEM-EDXS observations
754 previously discussed, that this source is still active, from direct brake pad abrasion, or from
755 leaching of ancient asphalt surfaces (Dong et al., 2017; Spreadbury et al., 2021).

756 Antimony speciation is driven by both biotic and abiotic geochemical processes including direct
757 Sb bacterial respiration (Li et al., 2016; Loni et al., 2019) and secondary Sb reduction by
758 reductants produced by bacterial respiration. For instance, antimony(V) reduction can be
759 caused by local production of electron donors such as Fe(II) or sulphides, themselves
760 biogenically produced in anoxic/suboxic conditions by Fe(III)-reducing or sulphide producing
761 bacteria. Fe(III)-oxy(hydro)xides bioreduction induces a release of Fe(II) into the water and a
762 precipitation of secondary Fe(III) bearing minerals (Burton et al., 2019, 2020). This precipitation
763 may cause the incorporation of Sb(V) species in the neofomed minerals *via* Fe(III) substitution
764 (Hockmann et al., 2021) or Sb(V) reduction to Sb(III) (Kirsch et al., 2008). Sb(V) reduction can
765 also be mediated by reduced organic matter such as humic acids when associated to Fe(II) in
766 solution (Karimian et al., 2019). In turn, sulphide produced by bacteria can result in Fe-
767 oxy(hydro)xides sulphidation followed by the release of Sb(III) and the subsequent formation
768 of Sb(III)-S species (Ye et al., 2019; Hockmann et al., 2020; Ye and Jing, 2022). Finally, abiotic
769 processes resulting from surface electrons transfer from Fe and Mn oxyhydroxides to Sb(III)
770 species under oxic atmosphere has been shown to occur at both acidic and neutral pH,
771 resulting in Sb(III) oxidation (Belzile et al., 2001).

772 No direct speciation data are currently available on Sb emitted from road dust contamination
773 when transferred to surrounding surface environments such as soils, sediments and
774 hydrosystems. In the studied pond systems, representative of surface accumulator media, two
775 distinct patterns were discernible. Indeed, solids sampled in oxic “dry” conditions present
776 exclusively oxygen-bound form of Sb, while an additional sulphur-bound form is observed for

777 suboxic underwater samples. This observation would support the hypothesis of local
778 biogeochemical transformations. This is in line with the results of Arsic et al. (2018) who
779 observed a significant contribution of Sb(III)-S species (25% to 60%) in their experiments of
780 anoxic sediment aged under a water column and with Ye and Jing (2022) showing the
781 immobilisation of Sb in the Sb_2S_3 form due to S(0) reduction by *Shewanella oneidensis* MR-1
782 in the presence of Sb(III) adsorbed goethite. Here, we observe an important contribution of
783 Sb(III)-S (48% to 80%) in the underwater samples. Since Sb_2S_3 is constitutive of brake pads,
784 we cannot exclude that part the measured Sb(III)-S contribution could originate directly from
785 Sb_2S_3 fragments even if its oxidation is mainly expected due to brake friction (Matějka et al.,
786 2011; Martinez and Echeberria, 2016). If produced by local biogeochemical reactions as
787 shown in the study of Arsic et al. (2018), in the present study, questions remain on the actual
788 identity of the Sb(III)-S phases present in our samples. Indeed, such a Sb(III)-S XANES
789 spectral contribution could be the signature of Sb bonding to thiol functional groups of organic
790 matter (OM) (Besold et al., 2019a, 2019b) or Sb(III) association with iron sulphide such as FeS
791 or FeS_2 (Kirch et al., 2008; Hockmann et al., 2020), or of amorphous Sb-sulphide as observed
792 elsewhere (Kulp et al., 2014; Bennett et al., 2017; Besold et al., 2019; Ye and Jing, 2022).

793 Thioantimonate species have been designated as potential intermediates of these sulphidation
794 reactions, having particular consequences on Sb mobility for instance by limiting Sb affinity to
795 iron oxides (Ye et al., 2019, 2021). The presence of minor amounts of such thio-Sb forms,
796 including within the solid phase, could not be excluded since XANES spectra of sorbed thio-
797 Sb at the Sb *K*-edge should contribute in between the Sb-O and Sb-S species. In the literature,
798 the sulphidation process of particles such as Sb(V)-containing oxyhydroxides has recently
799 been reported to result in an important Sb mobilization towards the aqueous phase, likely
800 resulting in Sb depletion in the solid fraction (Hockmann et al., 2020). Here, Sb concentrations
801 were on average lower in underwater samples compared to the ones sampled on surfaces
802 exposed to air, which would be in line with this process. Alternatively, this difference of

803 concentration could be due to dilution of Sb inputs by detrital particles accumulating in the
804 basins.

805 In underwater samples of the present study, no statistically significant contribution from
806 Sb(III)-O species were detected. In contrast, Arsic et al. (2018) have observed this species
807 even under anoxic conditions, and Besold et al. (2019a) also observed an important Sb(III)-O
808 contribution in peatland samples. In this latter study, the authors conclude that the high organic
809 content and/or the particular nature of OM would stabilize the Sb(III)-O form, which could also
810 be the case for Arsic et al. (2018). In their study concerning Fe oxyhydroxides sulphidation
811 experiments, Hockmann et al. (2020) observed a weak contribution of the Sb(III)-O species in
812 the solids, in particular in their low sulphidic system, which could be related to the fact that only
813 a negligible fraction of antimonite is detected in the aqueous phase.

814 In the underwater sample S-DBSO-1A10, situated upstream in the RR pond system, the major
815 species are Sb(III)-S ($84 \pm 10\%$) with only $16 \pm 10\%$ of Sb(V)-O, while in the dry sample
816 S-FBPI-1A10, located very close on the same hydrologic pathway but at the open air, our
817 results show 74% of Sb(V)-O and 26% of Sb(III)-O. This means that over a short spatial course,
818 Sb shows significant differences in its redox geochemistry. Thus, this would confirm that Sb
819 speciation is particularly versatile in such surface environments, likely driven by the local redox
820 potential. Indeed, changes from anoxic to oxic media result in dramatic changes of Sb oxidation
821 state and coordination chemistry. In addition, the fact that dry sample is more concentrated in
822 Sb than underwater sample would likely support the hypothesis of a Sb transfer, for instance
823 in the dissolved phase, and potentially resulting from release due to Sb sulphidation upstream
824 in the pond as evoked previously. These results raise questions about the mobility properties
825 of Sb at the liquid/solid interface in stormwater ponds, in particular because water fluctuations
826 often occur in these ponds, due to evaporation associated with long dry periods and storm
827 events or management operations.

828 5. Conclusion

829

830 This study brings new information about antimony isotope geochemistry and speciation in
831 stormwater pond accumulator media representative of surface environments impacted by road
832 runoff such as urban areas. Both semi-urban and rural ponds are observed to be contaminated
833 with a cocktail of inorganic contaminants clearly identified as emitted by road traffic (Cu, Zn,
834 Sb and Pb). Additional inorganic contaminants (Cd, Ni and Cr) are particularly observed in
835 urban ponds and their presence is interpreted to originate from anthropogenic urban/industrial
836 activities. The Pb isotope ratio dataset shows that the impact of urban areas is significant even
837 if the sampling sites are not directly connected to urban networks, which would reflect a
838 contamination at a larger scale, likely due to atmospheric particle inputs or to urban particles
839 reemitted by leaching of vehicles during rain events. Antimony is the most enriched element in
840 both rural and urban highway stormwater ponds exposed to the road traffic source. For the
841 first time, Sb isotope composition ($\delta^{123}\text{Sb}$) of road dust sediments is characterized and shows
842 a homogenous value among the different road-impacted sites, giving access to the mean
843 signature of the Sb-containing brake lining materials used in France during the decades.
844 Preliminary data obtained on both solid and dissolved phases at the rural site indicate that
845 $\delta^{123}\text{Sb}$ use as (bio)geochemical tracer is promising and should be further studied. Then, we
846 show that Sb is subjected to important changes of speciation (oxidation state and ligands) in
847 the road-to-pond waterway, and is thus highly sensitive to redox changes at the stormwater
848 pond scale. To this respect, a perspective of research is to study the geochemical reactivity of
849 Sb upon aging when the contaminated stormwater pond sediments are submitted to long
850 period of dryness. Thus, mobility of Sb from the main Sb-bearing phases observed should be
851 evaluated to help to manage this contamination. From the results presented here, we posit that
852 the processes leading to speciation and isotopic modifications should be studied in details for
853 a better management of Sb contamination in stormwater pond infrastructures and downstream
854 aquatic environments, and subsequently in urban surface environments exposed to road traffic
855 contaminations.

Journal Pre-proof

857 **Credit author statement**

858 **Maëva Philippe:** Conceptualization, Methodology, Investigation, Formal analysis, Writing -
859 Original Draft, Writing - Review & Editing - **Pierre Le Pape:** Conceptualization, Methodology,
860 Investigation, Formal analysis, Writing - Original Draft, Writing - Review & Editing, Supervision
861 - **Éléonore Resongles:** Investigation, Formal analysis, Writing - Review & Editing - **Gautier**
862 **Landrot:** Investigation, Software, Writing - Review & Editing - **Rémi Freydier:** Investigation,
863 Formal analysis - **Ludovic Delbes:** Investigation - **Louise Bordier:** Investigation, Formal
864 analysis, Writing - Review & Editing - **Benoît Baptiste:** Software, Investigation - **Camille Baya:**
865 Investigation - **Corinne Casiot:** Methodology, Writing - Review & Editing - **Sophie Ayrault:**
866 Conceptualization, Methodology, Investigation, Formal analysis, Writing - Original Draft,
867 Writing - Review & Editing, Project administration, Supervision.

868 **Acknowledgments**

869
870 We thank the SOLEIL Synchrotron for having provided beamtime. We are grateful to E. Elkaïm
871 for his help during XRD measurements of ferrihydrite reference compounds used in this study
872 at the CRISTAL beamline (BAG proposal) and to SAMBA beamline staff help during XANES
873 and EXAFS measurements. We thank the IMPMC SEM-FIB platform staff (Imène Estève,
874 Béatrice Doisneau, Stéphanie Delbrel), the DiRIF service and COFIROUTE company for
875 granting us access to their installations and all the necessary information about their
876 management. We thank Manon Stope for her help during the preparation of samples prior to
877 Sb isotope analysis and Colin Ferrari and Sophie Delpoux for their help during Sb analysis at
878 the AETE-ISO platform, (OSU-OREME/Université de Montpellier). This work was financially
879 supported by the CNRS EC2CO INSU program and the PIREN-Seine Program. This work has
880 been conducted in the framework of the PhD thesis of Maëva Philippe at Paris-Saclay
881 University (ED 579 SMEMaG).

882

883 **References**

- 884 Ahmed F. and Ishiga H. (2006) Trace metal concentrations in street dusts of Dhaka city,
885 Bangladesh. *Atmos. Environ.* 40, 3835–3844.
- 886 Amereih S., Meisel T., Scholger R. and Wegscheider W. (2005) Antimony speciation in soil
887 samples along two Austrian motorways by HPLC-ID-ICP-MS. *J. Environ. Monit.* 7, 1200–1206.
- 888 Arsic M., Teasdale P. R., Welsh D. T., Johnston S. G., Burton E. D., Hockmann K. and Bennett
889 W. W. (2018) Diffusive Gradients in Thin Films Reveals Differences in Antimony and Arsenic
890 Mobility in a Contaminated Wetland Sediment during an Oxic-Anoxic Transition. *Environ. Sci.*
891 *Technol.* 52, 1118–1127.
- 892 Avino P., Capannesi G. and Rosada A. (2008) Heavy metal determination in atmospheric
893 particulate matter by Instrumental Neutron Activation Analysis. *Microchem. J.* 88, 97–106.
- 894 Ayrault S., Roy-Barman M., Le Cloarec M.-F., Priadi C. R., Bonté P. and Göpel C. (2012) Lead
895 contamination of the Seine River, France: Geochemical implications of a historical perspective.
896 *Chemosphere* 87, 902–910.
- 897 Belzile N., Chen Y.-W. and Wang Z. (2001) Oxidation of antimony (III) by amorphous iron and
898 manganese oxyhydroxides. *Chem. Geol.* 174, 379–387.
- 899 Bennett W. W., Hockmann K., Johnston S. G. and Burton E. D. (2017) Synchrotron X-ray
900 absorption spectroscopy reveals antimony sequestration by reduced sulphur in a freshwater
901 wetland sediment. *Environ. Chem.* 14, 345–349.
- 902 Besold J., Eberle A., Noël V., Kujala K., Kumar N., Scheinost A. C., Pacheco J. L., Fendorf S.
903 and Planer-Friedrich B. (2019a) Antimonite Binding to Natural Organic Matter: Spectroscopic
904 Evidence from a Mine Water Impacted Peatland. *Environ. Sci. Technol.* 53, 10792–10802.
- 905 Besold J., Kumar N., Scheinost A. C., Lezama Pacheco J., Fendorf S. and Planer-Friedrich B.
906 (2019b) Antimonite Complexation with Thiol and Carboxyl/Phenol Groups of Peat Organic
907 Matter. *Environ. Sci. Technol.* 53, 5005–5015.

- 908 Burton E. D., Hockmann K., Karimian N. and Johnston S. G. (2019) Antimony mobility in
909 reducing environments: The effect of microbial iron(III)-reduction and associated secondary
910 mineralization. *Geochim. Cosmochim. Acta* 245, 278–289.
- 911 Burton E. D., Hockmann K. and Karimian N. (2020) Antimony Sorption to Goethite: Effects of
912 Fe(II)-Catalyzed Recrystallization. *ACS Earth Space Chem.* 4, 476–487.
- 913 Byrne P., Taylor K. G., Hudson-Edwards K. A. and Barrett J. E. S. (2017) Speciation and
914 potential long-term behaviour of chromium in urban sediment particulates. *J Soils Sediments*
915 17, 2666–2676.
- 916 Chan D. and Stachowiak G. W. (2004) Review of automotive brake friction materials.
917 *Proceedings of the Institution of Mechanical Engineers, Part D: J. Automob. Eng.* 218, 953–
918 966.
- 919 Chen J., Tan M., Li Yulan, Zheng J., Zhang Y., Shan Z., Zhang G. and Li Yan (2008)
920 Characteristics of trace elements and lead isotope ratios in PM_{2.5} from four sites in Shanghai.
921 *J. Hazard. Mater.* 156, 36–43. Cho M. H., Ju J., Kim S. J. and Jang H. (2006) Tribological
922 properties of solid lubricants (graphite, Sb₂S₃, MoS₂) for automotive brake friction materials.
923 *Wear* 260, 855–860.
- 924 Clozel B., Ruban V., Durand C. and Conil P. (2006) Origin and mobility of heavy metals in
925 contaminated sediments from retention and infiltration ponds. *Appl. Geochem.* 21, 1781–1798.
- 926 Davis A. P., Shokouhian M. and Ni S. (2001) Loading estimates of lead, copper, cadmium, and
927 zinc in urban runoff from specific sources. *Chemosphere* 44, 997–1009.
- 928 Degryse P., Lobo L., Shortland A., Vanhaecke F., Blomme A., Painter J., Gimeno D., Eremin
929 K., Greene J., Kirk S. and Walton M. (2015) Isotopic investigation into the raw materials of Late
930 Bronze Age glass making. *J. Archaeol. Sci.* 62, 153–160.
- 931 Dillis S., Ham-Meert A. V., Leeming P., Shortland A., Gobejishvili G., Abramishvili M. and
932 Degryse P. (2019) Antimony as a raw material in ancient metal and glass making:

- 933 provenancing Georgian LBA metallic Sb by isotope analysis. *STAR: Sci. Technol. Archaeol.*
934 *Res.* 0, 1–15.
- 935 Dong S., Ochoa Gonzalez R., Harrison R. M., Green D., North R., Fowler G. and Weiss D.
936 (2017) Isotopic signatures suggest important contributions from recycled gasoline, road dust
937 and non-exhaust traffic sources for copper, zinc and lead in PM₁₀ in London, United Kingdom.
938 *Atmos. Environ.* 165, 88–98.
- 939 Emmanuel S. and Erel Y. (2002) Implications from concentrations and isotopic data for Pb
940 partitioning processes in soils. *Geochim. Cosmochim. Acta* 66, 2517–2527.
- 941 Farmer J. G., Eades L. J., Atkins H. and Chamberlain D. F. (2002) Historical Trends in the
942 Lead Isotopic Composition of Archival Sphagnum Mosses from Scotland (1838–2000).
943 *Environ. Sci. Technol.* 36, 152–157.
- 944 Ferrari C., Méheut M., Resongles E., Freyrier R. and Casiot C. (2022) Equilibrium mass-
945 dependent isotope fractionation of antimony between stibnite and Sb secondary minerals: A
946 first-principles study. *Chem. Geol.* 611, 121115.
- 947 Ferrari C., Resongles E., Freyrier R. and Casiot C. (2021) A single-step purification method
948 for the precise determination of the antimony isotopic composition of environmental, geological
949 and biological samples by HG-MC-ICP-MS. *J. Anal. At. Spectrom.* 36, 776–785.
- 950 Filella M., Williams P. A. and Belzile N. (2009) Antimony in the environment: knowns and
951 unknowns. *Environ. Chem.* 6, 95.
- 952 Froger C., Ayrault S., Evrard O., Monvoisin G., Bordier L., Lefèvre I. and Quantin C. (2018)
953 Tracing the sources of suspended sediment and particle-bound trace metal elements in an
954 urban catchment coupling elemental and isotopic geochemistry, and fallout radionuclides.
955 *Environ. Sci. Pollut. Res.* 25, 28667–28681.

- 956 Froger C., Quantin C., Gasperi J., Caupos E., Monvoisin G., Evrard O. and Ayrault S. (2019)
957 Impact of urban pressure on the spatial and temporal dynamics of PAH fluxes in an urban
958 tributary of the Seine River (France). *Chemosphere* 219, 1002–1013.
- 959 Gonzalez R. O., Strekopytov S., Amato F., Querol X., Reche C. and Weiss D. (2016) New
960 Insights from Zinc and Copper Isotopic Compositions into the Sources of Atmospheric
961 Particulate Matter from Two Major European Cities. *Environ. Sci. Technol.* 50, 9816–9824.
- 962 Hares R. J. and Ward N. I. (1999) Comparison of the heavy metal content of motorway
963 stormwater following discharge into wet biofiltration and dry detention ponds along the London
964 Orbital (M25) motorway. *Sci. Total Environ.* 235, 169–178.
- 965 Haus N., Zimmermann S., Wiegand J. and Sures B. (2007) Occurrence of platinum and
966 additional traffic related heavy metals in sediments and biota. *Chemosphere* 66, 619–629.
- 967 Helmreich B., Hilliges R., Schriewer A. and Horn H. (2010) Runoff pollutants of a highly
968 trafficked urban road – Correlation analysis and seasonal influences. *Chemosphere* 80, 991–
969 997.
- 970 Hjortenkrans D., Bergbäck B. and Häggerud A. (2006) New Metal Emission Patterns in Road
971 Traffic Environments. *Environ. Monit. Assess.* 117, 85–98.
- 972 Hjortenkrans D. S. T., Bergbäck B. G. and Häggerud A. V. (2007) Metal Emissions from Brake
973 Linings and Tires: Case Studies of Stockholm, Sweden 1995/1998 and 2005. *Environ. Sci.*
974 *Technol.* 41, 5224–5230.
- 975 Hockmann K., Karimian N., Schlagenhauff S., Planer-Friedrich B. and Burton E. D. (2021)
976 Impact of Antimony(V) on Iron(II)-Catalyzed Ferrihydrite Transformation Pathways: A Novel
977 Mineral Switch for Ferrihydrite Formation. *Environ. Sci. Technol.*
- 978 Hockmann K., Planer-Friedrich B., Johnston S. G., Peiffer S. and Burton E. D. (2020) Antimony
979 mobility in sulfidic systems: Coupling with sulfide-induced iron oxide transformations. *Geochim.*
980 *Cosmochim. Acta* 282, 276–296.

- 981 Hu X., He M., Li S. and Guo X. (2017) The leaching characteristics and changes in the leached
982 layer of antimony-bearing ores from China. *J. Geochem. Explor.* 176, 76–84.
- 983 Hwang H.-M., Fiala M. J., Park D. and Wade T. L. (2016) Review of pollutants in urban road
984 dust and stormwater runoff: part 1. Heavy metals released from vehicles. *Int. J. Urban Sci.* 20,
985 334–360.
- 986 Ingo G. M., D’Uffizi M., Falso G., Bultrini G. and Padeletti G. (2004) Thermal and microchemical
987 investigation of automotive brake pad wear residues. *Thermochim. Acta* 418, 61–68.
- 988 Johansson C., Norman M. and Burman L. (2009) Road traffic emission factors for heavy
989 metals. *Atmos. Environ.* 43, 4681–4688.
- 990 Johnston S. G., Bennett W. W., Doriean N., Hockmann K., Karimian N. and Burton E. D. (2020)
991 Antimony and arsenic speciation, redox-cycling and contrasting mobility in a mining-impacted
992 river system. *Sci. Total Environ.* 710, 136354.
- 993 Kamalakkannan R., Zettel V., Goubatchev A., Stead-Dexter K. and Ward N. I. (2004) Chemical
994 (polycyclic aromatic hydrocarbon and heavy metal) levels in contaminated stormwater and
995 sediments from a motorway dry detention pond drainage system. *J. Environ. Monit.* 6, 175–
996 181.
- 997 Karimian N., Burton E. D., Johnston S. G., Hockmann K. and Choppala G. (2019) Humic acid
998 impacts antimony partitioning and speciation during iron(II)-induced ferrihydrite transformation.
999 *Sci. Total Environ.* 683, 399–410.
- 1000 Kibblewhite M. G. (2018) Contamination of agricultural soil by urban and peri-urban highways:
1001 An overlooked priority? *Environ. Pollut.* 242, 1331–1336.
- 1002 Kirsch R., Scheinost A. C., Rossberg A., Banerjee D. and Charlet L. (2008) Reduction of
1003 antimony by nano-particulate magnetite and mackinawite. *Miner. Mag.* 72, 185–189.
- 1004 Komárek M., Ettler V., Chrastný V. and Mihaljevič M. (2008) Lead isotopes in environmental
1005 sciences: A review. *Environ. Int.* 34, 562–577.

- 1006 Krachler M., Zheng J., Koerner R., Zdanowicz C., Fisher D. and Shotyk W. (2005) Increasing
1007 atmospheric antimony contamination in the northern hemisphere: snow and ice evidence from
1008 Devon Island, Arctic Canada. *J. Environ. Monit.* 7, 1169–1176.
- 1009 Kulp T. R., Miller L. G., Braiotta F., Webb S. M., Kocar B. D., Blum J. S. and Oremland R. S.
1010 (2014) Microbiological Reduction of Sb(V) in Anoxic Freshwater Sediments. *Environ. Sci.*
1011 *Technol.* 48, 218–226.
- 1012 Landrot G. (2018) FASTOSH: a software to process XAFS data for geochemical &
1013 environmental applications. In Goldschmidt. Boston. p. 1402.
- 1014 Le Pape P., Blanchard M., Brest J., Boulliard J.-C., Ikogou M., Stetten L., Wang S., Landrot G.
1015 and Morin G. (2017) Arsenic Incorporation in Pyrite at Ambient Temperature at Both
1016 Tetrahedral S–I and Octahedral FeII Sites: Evidence from EXAFS–DFT Analysis. *Environ. Sci.*
1017 *Technol.* 51, 150–158.
- 1018 Le Pape P., Ayrault S., Michelot J.-L., Monvoisin G., Noret A. and Quantin C. (2013) Building
1019 an isotopic hydrogeochemical indicator of anthropogenic pressure on urban rivers. *Chem.*
1020 *Geol.* 344, 63–72.
- 1021 Le Pape P., Ayrault S. and Quantin C. (2012) Trace element behavior and partition versus
1022 urbanization gradient in an urban river (Orge River, France). *J. Hydrol.* 472–473, 99–110.
- 1023 Lee W. K., Rhee T. H., Kim H. S. and Jang H. (2013) Effects of antimony trisulfide (Sb₂S₃) on
1024 sliding friction of automotive brake friction materials. *Met. Mater. Int.* 19, 1101–1107.
- 1025 Li J., Wang Q., Oremland R. S., Kulp T. R., Rensing C. and Wang G. (2016) Microbial Antimony
1026 Biogeochemistry: Enzymes, Regulation, and Related Metabolic Pathways. *Appl. Environ.*
1027 *Microbiol.* 82, 5482–5495.
- 1028 Liu K., Hou S., Wu S., Zhang W., Zou X., Yu J., Song J., Sun X., Huang R., Pang H. and Wang
1029 J. (2021) Assessment of heavy metal contamination in the atmospheric deposition during
1030 1950–2016 A.D. from a snow pit at Dome A, East Antarctica. *Environ. Pollut.* 268, 115848.

- 1031 Lobo L., Degryse P., Shortland A., Eremin K. and Vanhaecke F. (2013) Copper and antimony
1032 isotopic analysis via multi-collector ICP-mass spectrometry for provenancing ancient glass. J.
1033 Anal. At. Spectrom. 29, 58–64.
- 1034 Loni P. C., Wu M., Wang W., Wang H., Ma L., Liu C., Song Y. and H Tuovinen O. (2019)
1035 Mechanism of microbial dissolution and oxidation of antimony in stibnite under ambient
1036 conditions. J. Hazard. Mater., 121561.
- 1037 Martinez A. M. and Echeberria J. (2016) Towards a better understanding of the reaction
1038 between metal powders and the solid lubricant Sb₂S₃ in a low-metallic brake pad at high
1039 temperature. Wear 348–349, 27–42.
- 1040 Matějka V., Lu Y., Matějková P., Smetana B., Kukutschová J., Vaculík M., Tomášek V., Zlá S.
1041 and Fan Y. (2011) Possible stibnite transformation at the friction surface of the semi-metallic
1042 friction composites designed for car brake linings. Appl. Surf. Sci. 258, 1862–1868.
- 1043 Meland S., Borgstrøm R., Heier L. S., Rosseland B. O., Lindholm O. and Salbu B. (2010)
1044 Chemical and ecological effects of contaminated tunnel wash water runoff to a small
1045 Norwegian stream. Sci. Total Environ. 408, 4107–4117.
- 1046 Monna F., Lancelot J., Croudace I. W., Cundy A. B. and Lewis J. T. (1997) Pb Isotopic
1047 Composition of Airborne Particulate Material from France and the Southern United Kingdom:
1048 Implications for Pb Pollution Sources in Urban Areas. Environ. Sci. Technol. 31, 2277–2286.
- 1049 Moriwaki H., Kitajima S. and Katahira K. (2009) Waste on the roadside, ‘poi-sute’ waste: Its
1050 distribution and elution potential of pollutants into environment. Waste Manag. 29, 1192–1197.
- 1051 Napier F., D’Arcy B. and Jefferies C. (2008) A review of vehicle related metals and polycyclic
1052 aromatic hydrocarbons in the UK environment. Desalination 226, 143–150.
- 1053 Nielsen K., Kalmykova Y., Strömvall A.-M., Baun A. and Eriksson E. (2015) Particle phase
1054 distribution of polycyclic aromatic hydrocarbons in stormwater — Using humic acid and iron
1055 nano-sized colloids as test particles. Sci. Total Environ. 532, 103–111.

- 1056 Nory R. M., Figueiredo A. M. G., Souto-Oliveira C. E. and Babinski M. (2021) Urban
1057 contamination sources in tunnel dusts from São Paulo city: Elemental and isotopic
1058 characterization. *Atmos. Environ.* 254, 118188. Paleu V., Georgescu S., Baciú C., Istrate B.
1059 and Baciú E. R. (2016) Preliminary experimental research on friction characteristics of a thick
1060 gravitational casted babbitt layer on steel substrate. *IOP Conf. Ser.: Mater. Sci. Eng.* 147,
1061 012028.
- 1062 Perron M. A. C. and Pick F. R. (2020) Water quality effects on dragonfly and damselfly nymph
1063 communities: A comparison of urban and natural ponds. *Environ. Pollut.* 263, 114472.
- 1064 Priadi C., Bourgeault A., Ayrault S., Gourlay-Francé C., Tusseau-Vuillemin M.-H., Bonté P.
1065 and Mouchel J.-M. (2011) Spatio-temporal variability of solid, total dissolved and labile metal:
1066 passive vs. discrete sampling evaluation in river metal monitoring. *J. Environ. Monit.* 13, 1470–
1067 1479.
- 1068 Quiroz W., Cortés M., Astudillo F., Bravo M., Cereceda F., Vidal V. and Lobos M. G. (2013)
1069 Antimony speciation in road dust and urban particulate matter in Valparaíso, Chile: Analytical
1070 and environmental considerations. *Microchem. J.* 110, 266–272.
- 1071 Resongles E., Casiot C., Freydier R., Le Gall M. and Elbaz-Poulichet F. (2015a) Variation of
1072 dissolved and particulate metal(loid) (As, Cd, Pb, Sb, Tl, Zn) concentrations under varying
1073 discharge during a Mediterranean flood in a former mining watershed, the Gardon River
1074 (France). *J. Geochem. Explor.* 158, 132–142.
- 1075 Resongles E., Dietze V., Green D. C., Harrison R. M., Ochoa-Gonzalez R., Tremper A. H. and
1076 Weiss D. J. (2021) Strong evidence for the continued contribution of lead deposited during the
1077 20th century to the atmospheric environment in London of today. *Proc. Natl. Acad. Sci.* 118,
1078 e2102791118.
- 1079 Resongles E., Freydier R., Casiot C., Viers J., Chmeleff J. and Elbaz-Poulichet F. (2015b)
1080 Antimony isotopic composition in river waters affected by ancient mining activity. *Talanta* 144,
1081 851–861.

- 1082 Rouxel O., Ludden J. and Fouquet Y. (2003) Antimony isotope variations in natural systems
1083 and implications for their use as geochemical tracers. *Chem. Geol.* 200, 25–40.
- 1084 Salma I. and Maenhaut W. (2006) Changes in elemental composition and mass of atmospheric
1085 aerosol pollution between 1996 and 2002 in a Central European city. *Environ. Pollut.* 143, 479–
1086 488.
- 1087 Sánchez-Rodas D., Alsioufi L., Sánchez de la Campa A. M. and González-Castanedo Y.
1088 (2017) Antimony speciation as geochemical tracer for anthropogenic emissions of atmospheric
1089 particulate matter. *J. Hazard. Mater.* 324, 213–220.
- 1090 Sörme L. and Lagerkvist R. (2002) Sources of heavy metals in urban wastewater in Stockholm.
1091 *Sci. Total Environ.* 298, 131–145.
- 1092 Spreadbury C. J., Clavier K. A., Lin A. M. and Townsend T. G. (2021) A critical analysis of
1093 leaching and environmental risk assessment for reclaimed asphalt pavement management.
1094 *Sci. Total Environ.* 775, 145741.
- 1095 Stachel B., Holthuis J.-U., Schulz W., Seitz W., Weber W. H., Tegge K.-T. and Dobner I. (2010)
1096 Treatment Techniques and Analysis of Stormwater Run-off from Roads in Hamburg, Germany.
1097 In *Xenobiotics in the Urban Water Cycle: Mass Flows, Environmental Processes, Mitigation*
1098 *and Treatment Strategies* (Eds. D. Fatta-Kassinos, K. Bester, and K. Kümmerer). *Environ.*
1099 *Pollut.* Springer Netherlands, Dordrecht. pp. 445–461.
- 1100 Stechmann H and Dannecker W, 1990, Characterization and source analysis of vehicle-
1101 generated aerosols. *J. Aerosol Sci.* 21: S287–S290.
- 1102 Sun G., Wu Y., Feng X., Wu X., Li X., Deng Q., Wang F. and Fu X. (2021) Precise analysis of
1103 antimony isotopic composition in geochemical materials by MC-ICP-MS. *Chem. Geol.* 582,
1104 120459.
- 1105 Sutherland R. A. (2000) Bed sediment-associated trace metals in an urban stream, Oahu,
1106 Hawaii. *Environ. Geol.* 39, 611–627.

- 1107 Thévenot D. R., Moilleron R., Lestel L., Gromaire M.-C., Rocher V., Cambier P., Bonté P.,
1108 Colin J.-L., de Pontevès C. and Meybeck M. (2007) Critical budget of metal sources and
1109 pathways in the Seine River basin (1994–2003) for Cd, Cr, Cu, Hg, Ni, Pb and Zn. *Sci. Total*
1110 *Environ.* 375, 180–203.
- 1111 Thorpe A. and Harrison R. M. (2008) Sources and properties of non-exhaust particulate matter
1112 from road traffic: A review. *Sci. Total Environ.* 400, 270–282.
- 1113 Turner A. and Filella M. (2020) Antimony in paints and enamels of everyday items. *Sci. Total*
1114 *Environ.* 713, 136588.
- 1115 Varrica D., Bardelli F., Dongarrà G. and Tamburo E. (2013) Speciation of Sb in airborne
1116 particulate matter, vehicle brake linings, and brake pad wear residues. *Atmos. Environ.* 64,
1117 18–24.
- 1118 Von Uexküll O., Skerfving S., Doyle R. and Braungart M. (2005) Antimony in brake pads-a
1119 carcinogenic component? *J. Clean. Prod.* 13, 19–31.
- 1120 Wang D., Mathur R., Zheng Y., Qiu K. and Wu H. (2021) Redox-controlled antimony isotope
1121 fractionation in the epithermal system: New insights from a multiple metal stable isotopic
1122 combination study of the Zhaxikang Sb–Pb–Zn–Ag deposit in Southern Tibet. *Chem. Geol.*
1123 584, 120541.
- 1124 Wang Q., Zhang Q., Wu Y. and Wang X. C. (2017) Physicochemical conditions and properties
1125 of particles in urban runoff and rivers: Implications for runoff pollution. *Chemosphere* 173, 318–
1126 325.
- 1127 Weckwerth G. (2001) Verification of traffic emitted aerosol components in the ambient air of
1128 Cologne (Germany). *Atmos. Environ.* 35, 5525–5536.
- 1129 Ye L., Chen H. and Jing C. (2019) Sulfate-Reducing Bacteria Mobilize Adsorbed Antimonate
1130 by Thioantimonate Formation. *Environ. Sci. Technol. Lett.* 6, 418–422.

- 1131 Ye L. and Jing C. (2022) Iron(III) reducing bacteria immobilise antimonite by respiring
1132 elemental sulfur. *Geochem. Persp. Lett.* 21, 37–41.
- 1133 Ye L., Zhong W., Zhang M. and Jing C. (2021) New Mobilization Pathway of Antimonite:
1134 Thiolation and Oxidation by Dissimilatory Metal-Reducing Bacteria via Elemental Sulfur
1135 Respiration. *Environ. Sci. Technol.*
- 1136 Zhang H., Lombi E., Smolders E. and McGrath S. (2004) Kinetics of Zn Release in Soils and
1137 Prediction of Zn Concentration in Plants Using Diffusive Gradients in Thin Films. *Environ. Sci.*
1138 *Technol.* 38, 3608–3613.
- 1139 Zhou W., Zhou A., Wen B., Liu P., Zhu Z., Finckh Z. and Zhou J. (2022) Antimony isotope
1140 fractionation during adsorption on aluminum oxides. *J. Hazard. Mater.* 429, 128317.
- 1141

Denomination	GPS coordinates	Construction (year)	Type	Drained surface	Traffic per day (2017)	Presence of speed camera
Semi-urban, recent (SUR)	48.7115, 2.1863	~2000	Decantation	Urban + Road	54,187	Yes
Semi-urban, old (SUO)	48.6334, 2.2246 48.6320, 2.2292	1990s	Decantation	Road	56,595	Yes
Rural, recent (RR)	48.5120, 1.9072 48.5125, 1.9082	2012	Decantation + filtration	Road	42,225	No

Highlights:

- Highway stormwater ponds concentrate Sb contamination from road runoff
- Sb isotopic composition of stormwater pond sediments is close to that of road dusts
- Sb(V)-O, Sb(III)-O, and Sb(III)-S species occur in the road-to-pond continuum
- Sb(III)-S species are observed as a specific signature of underwater reduced samples
- Sb speciation changes along the waterway show the high geochemical reactivity of Sb

Journal Pre-proof

Declaration of interests

The authors declare that they have no known competing financial interests or personal relationships that could have appeared to influence the work reported in this paper.

The authors declare the following financial interests/personal relationships which may be considered as potential competing interests:

Journal Pre-proof